

A new dynamic slip approach for wall-modeled Large Eddy Simulations in a Consistent Discontinuous Galerkin Framework

Pratikkumar Raje¹†, Karthik Duraisamy¹

¹Department of Aerospace Engineering, University of Michigan, Ann Arbor, MI 48109

(Received xx; revised xx; accepted xx)

A wall-modeled large eddy simulation approach is proposed in a Discontinuous Galerkin (DG) setting, building on the slip-wall concept of Bae et al. (JFM'19) and the universal scaling relationship by Pradhan and Duraisamy (JFM'23). The effect of the order of the DG approximation is introduced via the length scales in the formulation. The level of under-resolution is represented by a slip Reynolds number and the model attempts to also incorporate the effects of the numerical discretization and the subgrid-scale model. The dynamic part of the new model is based on a modified form of Germano identity –performed on the universal scaling parameter– and is coupled with the dynamic Smagorinsky model. A sharp modal cut-off filter is used as the test filter for the dynamic procedure, and the dynamic model can be easily integrated into any DG solver. Numerical experiments on channel flows show that grid independence of the statistics is achievable and predictions for the mean velocity and Reynolds stress profiles agree well with the DNS, even with significant under-resolution. When applied to flows with separation and reattachment, the model also consistently predicts one-point statistics in the reverse flow and post-reattachment regions in good agreement with experiments. The performance of the model in accurately predicting equilibrium and separated flows using significantly under-resolved meshes can be attributed to several aspects that work synergistically: the optimal finite-element projection framework; the interplay of the scale-separation and numerical discretization within the DG framework; and the consistent dynamic procedures for subgrid and wall modeling.

Key words: Turbulent flows, Large Eddy Simulation, Wall-modeled LES, Dynamic procedure, Slip wall model

1. Introduction

Wall-bounded turbulent flows are of particular relevance to many engineering applications. Computational costs of large eddy simulations (LES) increase significantly with the increase in Reynolds number. This is especially true for flows at friction velocity (u_τ) based Reynolds number $Re_\tau > 10^3$ which is the range of Reynolds numbers relevant to industrial

† Email address for correspondence: praje@umich.edu

applications (Smits & Marusic 2013). A Direct Numerical Simulations (DNS) resolve all the relevant scales of motion and offers the highest possible fidelity (Moin & Mahesh 1998). However, substantial grid requirements along with time step limitations at high Reynolds numbers make DNS infeasible for computing flows of practical relevance. On the other hand, RANS models all the relevant scales of motion and places less restrictive demands on computational costs but offers a lower fidelity (Wilcox *et al.* 1998). It may not be a reliable tool for computing flows for which the turbulence models are not calibrated.

A wall-resolved (WR) LES resolves dynamically important energy carrying eddies and models the nearly universal and nearly isotropic small i.e. subgrid-scales (SGS) (Sagaut 2005). For a WRLES of a turbulent boundary layer at high Reynolds number, however, a vast majority of the computational resources have to be spent on the viscous and logarithmic layers since the grid point requirement for each of these layers scale as $O(\text{Re}_\tau^2)$ (Larsson *et al.* 2016). To alleviate this ‘near wall problem of LES’, wall modeled (WM) LES offers a practical solution, which aims to bypass the resolution of the inner layer of the turbulent boundary layers. In a WMLES, turbulent motions in the inner layer are modeled, whereas outer layer turbulent motions are resolved as in a conventional LES (Piomelli & Balaras 2002). Wall-stress models and hybrid LES/RANS are the two different approaches to model the inner layer and perform a WMLES. As these approaches still resolve the outer layer of the turbulent boundary layer, they can - in principle - offer better fidelity than RANS techniques.

A traditional wall-model estimates the filtered wall-shear stress at each time step based on a log-law, e.g. Reichardt’s profile (Reichardt 1951), using the LES information from the off-wall grid point on a LES mesh. The wall shear stress is then passed onto the LES grid as a Neumann boundary condition. The filtered velocity profile obtained using a traditional WMLES depends on the choice of the off-wall grid point from which the instantaneous LES solution is sampled to calculate the wall shear stress (Kawai & Larsson 2012). The commonly followed practice of feeding the instantaneous LES solution to the wall-model from the first off-wall grid point generally results in a positive (Kawai & Larsson 2012) or a negative (Cabot & Moin 2000) log-layer mismatch. A simple but effective approach to remove the log-layer mismatch, as shown by Kawai & Larsson (2012), is to fix the height of the modeled wall-layer and refine the grid. The method intends to reduce the error in the input to the wall-model and provide accurate well-resolved LES information to compute the wall shear stress.

A hybrid RANS/LES technique, including the detached eddy simulation (DES) in a WMLES set-up, uses RANS equations in the inner layer to estimate the wall stress and switches to the LES mode in the outer layer (Heinz 2020). The LES solution is used to feed information to a RANS model at some distance away from the wall. The predictions, however, depend on the choice of the RANS model and the modeling of the RANS/LES interface and generally suffer from the log-layer mismatch problem. Stochastic forcing (Piomelli *et al.* 2003; Davidson & Dahlström 2005; Davidson & Billson 2006; Keating & Piomelli 2006) and adjusting the blending function between the LES and RANS eddy-viscosities (Choi *et al.* 2009; Shur *et al.* 2008) can improve the results and reduce the log-layer mismatch. However, such strategies are strongly dependent on a number of parameters, e.g. the forcing amplitude and grid resolution (Larsson *et al.* 2016). Other efforts that seek to reduce the effects of SGS modeling errors and numerical errors due to the coarse near-wall grid resolution in a WMLES rely on techniques from optimal control theory (Nicoud *et al.* 2001; Templeton *et al.* 2006, 2008).

Accurate and reliable prediction of separated flows at high Reynolds numbers remains a pacing research issue within the CFD community. Several efforts to validate the state-of-the-art WMLES techniques in predicting separated flows at appropriate Reynolds numbers in a realistic external aerodynamics configuration have been undertaken recently. NASA CFD

Vision 2030 report Slotnick *et al.* (2014) has identified WMLES for complex 3D flows of practical relevance as one of the key milestones along the CFD technology development roadmap. Park & Moin (2016); Lehmkuhl *et al.* (2018); Goc *et al.* (2020, 2021) have investigated predictive capabilities of equilibrium and non-equilibrium models within the WMLES framework in the characterization of the flow around an aircraft by considering the JAXA Standard Model and NASA Common Research model with wing/body/tail configuration, showing promise in practical applications, yet identifying several areas of improvement.

Bose & Moin (2014) propose an alternative wall modeling approach to predict high Reynolds number flows involving boundary layer separation. It is based on the argument that the solution of the filtered Navier-Stokes equations would not necessarily provide a zero velocity at the wall, especially in the case of a coarse near-wall grid resolution. They proposed to replace the no-slip boundary condition used in conventional LES and WMLES with a boundary condition that allows for finite values of filtered velocity at the wall i.e. slip-velocity. Unlike traditional wall-stress models and hybrid RANS/LES approaches, the method does not use a wall-stress model or a RANS model in the inner layer to estimate the wall-stress. As a result, sampling of the LES solution at the off-wall grid points is not required. The slip wall model provides a method to estimate the slip velocity when the near wall solution is under-resolved. The model is derived using the properties of a modified form of the differential filter (Germano 1986), and it does not make any assumptions about the local state of the boundary layer or any RANS/LES hybridization.

The slip wall model relates the velocity field at the wall to the wall-normal derivative of the velocity field via a wall-adjacent length scale called as slip length. The slip length depends on a model coefficient C_w and the near-wall grid resolution Δ . The model recovers the no-slip condition as the near wall grid is refined and in the limit $\Delta \rightarrow 0$, and smoothly admits a wall slip velocity as the near wall grid resolution is coarsened and the flow is no longer fully resolved. The slip wall model is a general boundary condition applicable to any geometrically complex surface, including two orthogonally or non-orthogonally intersecting walls. Moreover, it is naturally suited to handle boundary layer separation as it will smoothly revert to a no-slip condition at the separation point without additional sensors or damping functions.

The value of the model parameter i.e. the slip length is found to depend on the Reynolds number Re_τ of the flow, grid resolution, SGS model, and the numerical discretization (Bae *et al.* 2019; Pradhan & Duraisamy 2023; Carton de Wiart & Murman 2017). Bose & Moin (2014) proposed a dynamic procedure to calculate the slip length based on the Germano's identity. However, attempts to reproduce the results for a high Re_τ channel flow were unsuccessful (Bae *et al.* 2019). The wall-stress invariant dynamic wall model (WSIM) of Bae *et al.* (2019) provides an alternate dynamic procedure to estimate the slip length. The model predictions for the channel flow at the high Re_τ cases are found to depend on the grid resolution, and grid convergence studies were not carried out. Numerical experiments with different prescribed values of slip length using NASA's discontinuous-Galerkin (DG) solver *eddy* in the implicit LES set-up failed to yield stable computations when applied to a channel flow at $Re_\tau \gtrsim 1000$ with a high order polynomial basis ($p = 3$ and $p = 7$).

Pradhan & Duraisamy (2023) employed an optimal finite-element projection framework to obtain *a priori* estimates of the wall slip velocity for a typical WMLES using DNS data for a channel flow (Lee & Moser 2015) and propose improvements to the slip wall model of Bose & Moin (2014). The optimal projection framework is used to modify the slip length, and it is represented as a function of the Reynolds number based on local slip velocity magnitude and near-wall local grid resolution Re_{slip} . A new model parameter λ is introduced to represent the effect of the numerical method or the order of projection p in the DG set-up and SGS

model. Using an *a priori* estimate for λ , the Re_{slip} model for the modified slip length is shown to give good predictions for a range of high Re_τ channel flow cases with the constant coefficient Smagorinsky SGS model using a DG solver with orders of projection up to $p = 3$.

The present study begins with the modified form of the slip wall model proposed by Pradhan & Duraisamy (2023) which uses the Re_{slip} model for the modified model coefficient. The main objective is to establish a dynamic modeling procedure for the model parameters. We use the dynamic Smagorinsky model (Germano *et al.* 1991) as the SGS model. The choice of the SGS is found to be critical to obtain the correct slope of the velocity profile in the log layer (Bae *et al.* 2019). On the other hand, values of the slip length are found to be responsible for a shift in the mean velocity profile relative to the DNS data, and they do not affect the shape of the mean velocity profile.

The manuscript is organized as follows. Section 2 presents the discontinuous Galerkin discretization framework used in the present work. Section 3 provides an overview of the original slip wall model formulation by Bose & Moin (2014) along with the modification introduced by Pradhan & Duraisamy (2023). The dynamic modeling procedures of Bose & Moin (2014) and Bae *et al.* (2019) to calculate the slip length are discussed briefly in Section 4. The proposed dynamic modeling strategy to estimate the model parameter λ using a modified form of Germano identity and the Re_{slip} model is presented in Section 5. The key assumptions to arrive at the final form of the dynamic model are also discussed. The proposed dynamic slip wall model is tested on a range of channel and periodic hill flows in Section 6 and results are compared with the available DNS and experimental data along with an equilibrium wall-stress model. Finally, conclusions are drawn in Section 7.

2. Discontinuous Galerkin discretization

The governing equations in this work are the compressible Navier-Stokes equations in their conservative form written as

$$\frac{\partial \mathbf{U}}{\partial t} + \nabla \cdot \mathbf{F}(\mathbf{U}) - \nabla \cdot \mathbf{G}(\mathbf{U}, \nabla \mathbf{U}) = \mathbf{0}, \quad (2.1)$$

where $\mathbf{U} \in \mathbb{R}^s$ is the conservative state vector of rank s , consisting of density, momentum, and total energy components, \mathbf{F} is the inviscid flux, and \mathbf{G} is the viscous flux. We note that boldface denotes a state vector. We use the Discontinuous Galerkin (DG) method for the spatial discretization. The DG method combines the concepts of finite element and finite volume methods and allows for high-order approximations, geometric flexibility, and natural parallelization. The computational domain Ω is divided into non-overlapping elements K , each having a sub-domain Ω_K and boundary $\partial\Omega_K$. These elements can have arbitrary shapes and sizes, allowing for efficient representation of complex geometries. A polynomial approximation is typically used to represent the solution using a L_2 -projection within each element. The degree of the polynomial p can vary, and higher-degree polynomials enable higher-order accuracy. The DG space \mathcal{V}_h is defined as

$$\mathcal{V}_h \triangleq \left\{ \phi \in L_2(\Omega) : \phi_h \equiv \phi|_{\Omega_K} \in P^p, \forall \Omega_K \in \Omega \right\}, \quad (2.2)$$

where the space of polynomials up to degree p is denoted as P^p , and ϕ_h is the basis function defined on Ω_K . Defining \mathcal{V}_h in this manner allows for discontinuities in the solution across element boundaries. The element-wise solution \mathbf{U}_h that approximates \mathbf{U} in Ω_k takes the form

$$\mathbf{U}(\mathbf{x}, t) \approx \mathbf{U}_h(\mathbf{x}, t) = \sum_{j=1}^{n_p} \mathbf{W}_{k,j}(t) \phi_{k,j}(\mathbf{x}), \quad \mathbf{x} \in \Omega_k, \quad (2.3)$$

where $\mathbf{U}_{k,j}$ represents the coefficients associated with the j^{th} basis function $\phi_{k,j}$ and n_p represents the total number of degrees of freedom within the element k of order p .

The DG method employs a weak formulation of the governing equations which is obtained by multiplying Eqn. (2.1) by test functions, which are the same as the basis functions, integrating by parts, and coupling the elements via numerical fluxes,

$$\begin{aligned} \int_{\Omega_K} \phi_h^T \frac{\partial \mathbf{U}_h}{\partial t} d\Omega - \int_{\Omega_K} \nabla \phi_h^T \cdot [\mathbf{F}(\mathbf{U}_h) - \mathbf{G}(\mathbf{U}_h, \nabla \mathbf{U}_h)] d\Omega + \\ \int_{\partial\Omega_K} \phi_h^T \left[\widehat{\mathbf{F}}(\mathbf{U}_h^+, \mathbf{U}_h^-) - \widehat{\mathbf{G}}(\mathbf{U}_h^+, \mathbf{U}_h^-, \nabla \mathbf{U}_h^+, \nabla \mathbf{U}_h^-) \right] \cdot \mathbf{n} dS \\ - \int_{\partial\Omega_K} (\mathbf{U}_h^+ - \{\mathbf{U}_h\})^T \mathbf{G}(\mathbf{U}_h^+, \nabla \phi_h^+) \cdot \mathbf{n} dS = \mathbf{0}, \quad \forall \phi_h \in \mathcal{V}_h. \end{aligned} \quad (2.4)$$

$\partial\Omega_K$ represents the element boundary, and on that boundary, $(\cdot)^+$ and $(\cdot)^-$ represent quantities taken from the current and neighboring element, respectively. Approximate numerical fluxes are denoted by $\widehat{(\cdot)}$, $\{\cdot\}$ represents a face average or boundary value, and \mathbf{n} is the outward pointing normal vector. The boundary conditions are set through the numerical fluxes.

Substituting Eqn. (2.3) into Eqn. (2.4), we get the final update equation which can be written as,

$$\mathbf{M} \frac{d\mathbf{W}}{dt} = -\mathbf{RHS}, \quad (2.5)$$

where \mathbf{M} is the spatial mass matrix and \mathbf{RHS} consists of the volume and surface integrals. Then, the spatial residual vector can be defined as

$$\mathbf{R} \equiv \frac{d\mathbf{W}}{dt} = -\mathbf{M}^{-1} \mathbf{RHS}, \quad (2.6)$$

We solve for the expansion coefficients \mathbf{W} which then provide an approximation of the solution to the governing equations over the entire computational domain. The solver used in the present study is discussed in Section 6 and Appendix A.

3. Slip-wall modeling

The slip wall model is essentially a wall boundary condition. The main idea is that the slip velocity is a natural consequence of the near wall under-resolution of the LES mesh. This has also been shown by Pradhan & Duraisamy (2023) using the optimal finite-element projection framework wherein the L_2 projection of channel flow DNS data onto grids suitable for a WMLES result in slip velocities at the wall. Also, the magnitude of the slip velocity is shown to increase with an increase in near-wall grid under-resolution. This shows that the near equivalence in the boundary conditions for the unfiltered and filtered variables does not hold in the case of a coarse LES when wall modeling becomes necessary. A slip wall model is an alternative to the traditional wall-stress modeling approach wherein the wall stress is not estimated directly but is indirectly affected through the non-vanishing filtered velocities at the wall. It provides estimates of the slip velocities at the wall when the LES grid resolution is insufficient to accurately resolve the near-wall region and the no-slip condition is not satisfied.

Bose & Moin (2014) use the properties of a modified differential filter to derive a slip velocity boundary condition given as

$$\bar{u}_i = \bar{C}_w \bar{\Delta}_w \frac{\partial \bar{u}_i}{\partial n}, \quad (3.1)$$

where n is the wall-normal direction, \bar{C}_w is a tunable model coefficient, whereas $\bar{\Delta}_w$ is related to the near-wall grid resolution. In Eqn. (3.1), the slip velocity only depends on the wall-normal derivative of the velocity field and is a direct consequence of the constraint placed on the differential filter that the slip length vanishes at the boundaries. The magnitude of the slip length i.e. $\bar{C}_w \bar{\Delta}_w$ imposes a filter length scale at the wall; if it vanishes at the wall, then the filtered velocity field will exactly satisfy a no-slip boundary condition. The slip wall boundary condition smoothly admits a wall slip velocity as the near-wall LES resolution is coarsened and the flow is no longer fully resolved. It is pertinent to note that while Eqn. (3.1) is derived from a specific choice of the form of the filter kernel, previous studies (Pradhan & Duraisamy 2023; Carton de Wiart & Murman 2017) show that the slip wall model can still perform well even without using the specified filter explicitly.

Pradhan & Duraisamy (2023) characterize the wall slip velocity in a WMLES in terms of a Reynolds number based on slip velocity magnitude and near-wall under-resolution using the optimal finite-element projection framework and propose a modified form of the slip wall model given by

$$\bar{u}_i = \frac{\bar{C}_{w,\lambda}}{\lambda} \bar{\Delta}_w \frac{\partial \bar{u}_i}{\partial n}, \quad \text{where } \bar{C}_w = \frac{\bar{C}_{w,\lambda}}{\lambda}. \quad (3.2)$$

The model coefficient $\bar{C}_{w,\lambda}$ is a function of the slip-velocity based Reynolds number \bar{Re}_{slip} and λ , where $\bar{Re}_{slip} = \bar{u}_s (\bar{\Delta}_w^e / p) / \bar{\nu}$. Here, \bar{u}_s is the magnitude of the wall slip velocity, and $\bar{\nu}$ is the kinematic viscosity of the fluid. Note that, p denotes the order of polynomial basis used in the DG solver with $\bar{\Delta}_w^e$ being the element size adjacent to the wall, and their ratio represents the effective grid size. The model parameter λ contains the effect of the order of projection p and hence the numerical method along with the SGS model. Using the above form of $\bar{C}_{w,\lambda}$, it is found that given a SGS model $\bar{C}_{w,\lambda}/\lambda$ admits a universal scaling relationship for a particular value of λ for a wide range of the parameter space. As a result, the model incorporates the effect of Reynolds number, near-wall grid under-resolution, SGS model, and numerical discretization.

4. Previous dynamic slip-wall models

Bose & Moin (2014) presented a dynamic procedure to compute the slip length ($\bar{C}_w \bar{\Delta}_w$) in the slip wall model given by Eqn. (3.1). It uses a modified form of Germano's identity, which represents the invariance of the total Reynolds stress at the test-filtered level. The model coefficient ($\bar{C}_w \bar{\Delta}_w$) is computed as

$$\left(\bar{C}_w \bar{\Delta}_w\right)^2 \Delta_R^2 \frac{\widehat{\partial \bar{u}_i}}{\partial n} \frac{\widehat{\partial \bar{u}_j}}{\partial n} + T_{ij} - \widehat{\tau}_{ij} = \widehat{\bar{u}_i \bar{u}_j} - \widehat{\bar{u}_i} \widehat{\bar{u}_j}, \quad (4.1)$$

where $\Delta_R = (\widehat{\bar{\Delta}_w} / \bar{\Delta}_w)$ is the ratio of the test filter width to the grid filter width at the wall, and a value of $\Delta_R = 1.4$ is recommended. Here, $\widehat{(\cdot)}$ represents a grid filtered quantity, a hat, i.e., $\widehat{(\cdot)}$ denotes the test filtering operation, T_{ij} and τ_{ij} depict the SGS stress tensors at the test and grid filter levels, respectively. The slip length is assumed to be equal for the three spatial directions. Eqn. (4.1) is solved for $\left(\bar{C}_w \bar{\Delta}_w\right)$ using a least squares method. The model was tested on a series of high Reynolds number channel flows and NACA 4412 airfoil at near-stall conditions.

Bae *et al.* (2019) proposed an alternate dynamic modeling strategy for the slip length $\left(\bar{C}_w \bar{\Delta}_w\right)$ as an improvement over the Bose & Moin (2014) dynamic model. The dynamic

model is based on a combination of the invariance of wall stress condition under test filtering and a modified form of Germano's identity and is referred to as the wall-stress invariant model (WSIM). The proposed dynamic modeling approach, however, is not unique, and different modeling choices are possible. The dynamic model is given by

$$\left(\overline{C_w \Delta_w}\right)^2 = \frac{L_{ij} M_{ij} + F_{ij} M_{ij}}{M_{kl} M_{kl}}, \quad (4.2)$$

where

$$L_{ij} = \overline{u_i u_j} - \widehat{u_i u_j}, \quad (4.3)$$

$$M_{ij} = \left[\frac{\partial \overline{u_i}}{\partial n} \frac{\partial \overline{u_j}}{\partial n} - \Delta_R^2 \frac{\partial \widehat{u_i}}{\partial n} \frac{\partial \widehat{u_j}}{\partial n} \right], \quad (4.4)$$

and F_{ij} contains different wall stresses, namely Reynolds stress, subgrid stress, viscous stress, and pressure tensors computed from the specified velocity field. The model was tested on a statistically stationary plane turbulent channel, a non-equilibrium three-dimensional transient channel, and a zero-pressure-gradient flat-plate turbulent boundary layer.

5. A new dynamic slip-wall model

We propose a dynamic procedure to compute the model coefficient λ in the modified slip wall model given by Eqn. (3.2) rather than the slip length in Eqn. (3.1) following insights from Pradhan & Duraisamy (2023). We start with the Germano identity (Germano 1990), which can be written as

$$T_{ij} - \widehat{\tau}_{ij} = \widehat{\overline{u_i u_j}} - \widehat{u_i u_j}, \quad (5.1)$$

where the SGS stresses at the grid and test filtered levels are given by

$$\tau_{ij} = \overline{u_i u_j} - \overline{u_i u_j}, \quad \text{and} \quad T_{ij} = \widehat{\overline{u_i u_j}} - \widehat{u_i u_j}. \quad (5.2)$$

Eqn. (5.1) represents an exact identity and does not involve any assumptions. Subtracting $(\widehat{\overline{u_i u_j}} - \widehat{u_i u_j})$ from both sides of Eqn. (5.1), we get

$$T_{ij} - \widehat{\tau}_{ij} - (\widehat{\overline{u_i u_j}} - \widehat{u_i u_j}) = \overline{u_i u_j} - \widehat{u_i u_j} \quad (5.3)$$

We assume that the slip velocity at the test filtered level takes a form similar to that for the grid filtered level, and it is given by

$$\widehat{u_i} = \widehat{C_w \Delta_w} \frac{\partial \widehat{u_i}}{\partial n}, \quad (5.4)$$

where the model coefficient $\widehat{C_w} = \widehat{C_w, \lambda} / \lambda$ has a form similar to that of coefficient at the grid filtered level $\overline{C_w} = \overline{C_w, \lambda} / \lambda$. Next, we assume that λ is constant between the grid and test filtered levels. Another important assumption inherent to the form of Eqn. (5.4) is that the slip length is considered the same for the three spatial directions following the works of Bose & Moin (2014) and Bae *et al.* (2019). The model coefficient $\widehat{C_w, \lambda}$ is assumed to be a function of Reynolds number based on slip velocity magnitude and the near-wall grid resolution at the test filtered level along with λ . Substituting for the slip velocities at the grid filtered level and test filtered level using Eqn. (3.1) and Eqn. (5.4) in the right-hand-side of Eqn. (5.3), we get

$$\left(\overline{C_w \Delta_w}\right)^2 \frac{\partial \overline{u_i}}{\partial n} \frac{\partial \overline{u_j}}{\partial n} - \left(\widehat{C_w \Delta_w}\right)^2 \frac{\partial \widehat{u_i}}{\partial n} \frac{\partial \widehat{u_j}}{\partial n} = \overline{u_i u_j} - \widehat{u_i u_j}. \quad (5.5)$$

Now, $\bar{\Delta}_w$ and $\widehat{\Delta}_w$ depend on the grid resolution, p , and the filter used. On the other hand, the model coefficients \bar{C}_w and \widehat{C}_w depend on Re_{slip} , p at the grid and test filtered levels, respectively and the model coefficient λ . In principle, we can use the above equation to find λ for a given model for \bar{C}_w and hence \widehat{C}_w . However, this would result in a significantly complex non-linear equation in λ . We choose an alternate approach to simplify the process with an aim to keep a balanced mixture of physical content and mathematical simplicity and rewrite Eqn. (5.5) as

$$\left(\bar{C}_w \bar{\Delta}_w\right)^2 \left[\frac{\partial \bar{u}_i}{\partial n} \frac{\partial \bar{u}_j}{\partial n} - C_{wR}^2 \Delta_R^2 \frac{\partial \widehat{u}_i}{\partial n} \frac{\partial \widehat{u}_j}{\partial n} \right] = \bar{u}_i \bar{u}_j - \widehat{u}_i \widehat{u}_j, \quad (5.6)$$

where $C_{wR} = \widehat{C}_w / \bar{C}_w$ and $\Delta_{wR} = \widehat{\Delta}_w / \bar{\Delta}_w$. In this work, we use the value for Δ_w as per Pradhan & Duraisamy (2023) and Δ_{wR} is given by

$$\Delta_{wR} = \frac{\widehat{\Delta}_w}{\bar{\Delta}_w} = \frac{p}{p^\star}, \quad (5.7)$$

where p^\star is the sharp modal cut-off filter order, as discussed in Appendix A. On the other hand, Pradhan & Duraisamy (2023) show that the model coefficient $C_{w,\lambda}$ is a function of grid resolution, and its value increases when the grid resolution is changed from Δ^+ to $2\Delta^+$. In other words, given that the test filter width is coarser than the grid filter width, \widehat{C}_w can be expected to be greater than \bar{C}_w , thereby resulting in the ratio C_{wR} to be greater than one. We use a value of $C_{wR} = 2$ in this work. Sensitivity studies using different plausible values of C_{wR} are shown in Appendix C.

Let

$$M_{ij} = \left[\frac{\partial \bar{u}_i}{\partial n} \frac{\partial \bar{u}_j}{\partial n} - C_{wR}^2 \Delta_R^2 \frac{\partial \widehat{u}_i}{\partial n} \frac{\partial \widehat{u}_j}{\partial n} \right] \quad \text{and} \quad L_{ij} = \bar{u}_i \bar{u}_j - \widehat{u}_i \widehat{u}_j \quad (5.8)$$

for notational convenience. Eqn. (5.6) can then be equivalently written as

$$\left(\frac{\bar{C}_{w,\lambda}}{\lambda} \bar{\Delta}_w \right)^2 M_{ij} = L_{ij}. \quad (5.9)$$

Eqn. (5.9) represents six independent equations in space for a single unknown λ given the model for $\bar{C}_{w,\lambda}$. Thus, the system is overdetermined, and we use the method of least squares to obtain λ , which is then given by

$$\left(\frac{\bar{C}_{w,\lambda}}{\lambda} \bar{\Delta}_w \right)^2 = \max \left(\frac{\langle L_{ij} M_{ij} \rangle}{\langle M_{kl} M_{kl} \rangle}, 0 \right), \quad (5.10)$$

where $\langle \rangle$ indicates that the numerator and denominator are first averaged over an element followed by an averaging over the directions of homogeneity i.e. stream-wise and span-wise in case of channel flows and span-wise in case of periodic flows, and the ratio is clipped to have a maximum value of zero. We can rewrite the above equation as

$$\frac{\bar{C}_{w,\lambda}}{\lambda} \bar{\Delta}_w - l_s = 0, \quad (5.11)$$

where

$$l_s = \sqrt{\max\left(\frac{\langle L_{ij}M_{ij} \rangle}{\langle M_{kl}M_{kl} \rangle}, 0\right)}. \quad (5.12)$$

Pradhan & Duraisamy (2023) provide a model fit for $\bar{C}_{w,\lambda}$ based on L_2 projected channel flow DNS data, which is given by

$$\bar{C}_{w,\lambda} = \begin{cases} 0.725 \log_{10}\left(\frac{\overline{Re}_{slip}}{\lambda}\right) - 0.925, & \text{if } \log_{10}\left(\frac{\overline{Re}_{slip}}{\lambda}\right) > 4.25 \\ 0.6 \log_{10}\left(\frac{\overline{Re}_{slip}}{\lambda}\right) - 0.41, & \text{if } \log_{10}\left(\frac{\overline{Re}_{slip}}{\lambda}\right) > 3.18 \\ 0.475 \log_{10}\left(\frac{\overline{Re}_{slip}}{\lambda}\right) - 0.003, & \text{if } \log_{10}\left(\frac{\overline{Re}_{slip}}{\lambda}\right) > 0.7 \\ 0.33, & \text{otherwise.} \end{cases} \quad (5.13)$$

Substituting for $\bar{C}_{w,\lambda}$ in Eqn. (5.11), we get a non-linear equation with λ as the only unknown, which can be found dynamically using a numerical method. The Secant method is used to find λ using Eqns. (5.11) and (5.13). The parameter λ , thus obtained, can reach unrealistically high values, especially at high Reynolds numbers on coarse near-wall LES meshes. We prescribe an upper limit to λ as

$$\lambda_f = \max(\lambda, 3\lambda_{CCSM}), \text{ where } \lambda_{CCSM} = 1.125. \quad (5.14)$$

Here, λ_{CCSM} is the value of λ for the constant coefficient Smagorinsky model obtained using the optimal finite element projection framework in Pradhan & Duraisamy (2023). Finally, we use λ_f in Eqn. (3.2).

We remark that the dynamic modeling procedure to obtain λ as discussed above is not unique. The model coefficient can be obtained using a number of modeling choices e.g. modified form of the Germano identity used in Bae *et al.* (2019). Eqn. (5.10) has a form similar to that of the dynamic model of Bae *et al.* (2019), but it does not contain the additional wall-stress terms in the numerator, which originates from the invariance of wall-stress condition under test filtering. Those additional wall-stress terms are expected to predict the same wall stress regardless of the grid resolution (or filter) and act as an effective self-regulating mechanism to control the changes in slip length to predict the correct wall stress. In our case, a similar effect is obtained by enforcing the Pradhan & Duraisamy (2023) model for $\bar{C}_{w,\lambda}$.

5.1. Implementation of the wall boundary condition

We assume that there is no transpiration and slip is only allowed in the wall-parallel directions. It is useful to note that, the slip-wall model allows for transpiration as considered in the previous studies of Bose & Moin (2014), Bae *et al.* (2019), and Carton de Wiart & Murman (2017). However, using the optimal finite-element projection framework, Pradhan & Duraisamy (2023) show that the slip length associated with the wall-normal velocity is approximately zero. Hence, it can be set to zero without significant loss of generalizability. In the current implementation of the dynamic slip-wall model, we compute the wall-normal derivatives of the slip-velocity components at the wall using Eqn. (3.2). The wall-parallel slip-velocity components at the wall are computed using the solution inside the element adjacent to the wall. This is then used to compute the wall stress and it is applied as a Neumann boundary condition complemented by a slip boundary condition for the velocity. The numerical implementation is done using the following steps:

- At every integration point, a ghost value is created, where the wall-parallel slip-velocity

components at the wall are obtained from the element interior state \mathbf{U}_h^+ as

$$\bar{u}_{h,i}^b = \bar{u}_{h,i}^+ - \bar{u}_{h,j}^+ n_j n_i. \quad (5.15)$$

Wall-normal velocity gradients are also calculated using the interior solutions.

- Slip-wall parameters $C_{w,\lambda}$ and λ are computed using the dynamic slip-wall model.
- The wall-normal derivatives of the slip-velocity components at the wall are then computed using the slip-wall model given by Eqn. (3.2) as follows:

$$\left. \frac{\partial \bar{u}_{h,i}}{\partial n} \right|_w = \frac{\bar{u}_{h,i}^b}{\Delta(C_{w,\lambda}/\lambda)}, \quad (5.16)$$

- Finally, wall stress components at the quadrature points of the boundary faces are computed using the following formula:

$$\tau'_w = (\nu + \nu_{SGS}) \left. \frac{\partial \bar{u}_{h,i}}{\partial n} \right|_w, \quad (5.17)$$

where we consider the contribution of the mean wall stress from the viscous and the sub-grid stresses for the wall stress.

- The projected wall stress $\tau_{w,i} = \tau'_w n_i$ is applied as a Neumann boundary condition.

6. Numerical experiments.

In this work, we use CaslabDG, an in-house Discontinuous-Galerkin (DG) solver for the computations. The governing equations are the filtered compressible Navier-Stokes equations in conservative form. The solver was successfully used previously to compute statistically stationary channel flows at high Re_τ (Pradhan & Duraisamy 2023) using a constant coefficient Smagorinsky model with up to 3 orders of the polynomial basis p . The solver is parallelized using Message Passing Interface (MPI). Inviscid fluxes are approximated using Roe approximate Riemann solver (Roe 1981). An SGS model is used for the unresolved SGS stresses in the filtered Navier-Stokes equations. The SGS viscosity is added to the molecular viscosity and the viscous flux contains both molecular and turbulence contributions. The second form of Bassi and Rebay (Bassi & Rebay 2000), popularly known as the BR-2 scheme, is used for the viscous fluxes. The governing equations are marched in time using an explicit third-order Runge-Kutta TVD (RK3-TVD) scheme.

The solver uses the Lagrange nodal basis evaluated at the Gauss-Legendre quadrature points and the number of quadrature points ngp in each of the three directions is related to the polynomial degree of approximation by $ngp = (p + 2)$. The integrals are approximated using the Gauss quadrature rule. The basis and test functions are created using a tensor product of the one-dimensional Lagrange interpolating polynomials which forms a non-hierarchical nodal basis. The corresponding number of degrees of freedom in each element is $(p + 1)^3$. We use a Lagrange polynomial basis of degree $p = 2$ for all the wall-modeled LES computations. It is to be noted that we do not use an explicit filter for the spatial filtering operation, but rely on implicit filtering through the numerical discretization and grid resolution. Also, the polynomial basis degree of $p = 2$ used in this work does not warrant for polynomial dealiasing, which can be achieved by explicitly filtering the solution at every time step (Diosady & Murman 2013; Gassner & Beck 2013; Brazell *et al.* 2015).

The results obtained using the dynamic slip-wall model are compared with those obtained using an equilibrium wall-stress model (EQWM). For the EQWM, we compute the wall friction τ_w from the instantaneous velocity taken at the furthest distance from the wall inside the first element. The computed wall friction is then used as the Neumann boundary condition

applied at the quadrature points of the boundary faces. Our implementation is similar to the work of Carton de Wiart & Murman (2017). We use the Reichardt function of the form

$$u^+ = \frac{1}{\kappa} \ln(1 + \kappa z^+) + 6.646 \left[1 - \exp\left(\frac{-z^+}{11}\right) - \frac{z^+}{11} \exp\left(\frac{-z^+}{3}\right) \right], \quad (6.1)$$

where $\kappa = 0.38$, as the equilibrium wall-stress model, and use the Newton-Raphson method to iterate on the values of u^+ and y^+ . This wall function supports the theoretical velocity profile down to the wall. We have chosen this approach for its simplicity and efficiency, and it is shown to give excellent results for statistically steady channel flows at high Reynolds numbers in Carton de Wiart & Murman (2017).

6.1. Sharp modal cut-off filter as a test filter

The dynamic modeling procedure requires filtering at two different levels i.e. grid filter and test filter to calculate the value of the model coefficient λ . In a DG framework, this is equivalent to using two different orders of polynomial basis for approximating the solution. The Lagrange interpolation polynomials, which are used as the basis functions within our work, are not hierarchical i.e. every basis function contains high-order solution content. As a result, unlike a spectral method, we cannot directly use a sharp cut-off filter to remove the higher-order modes. To reduce the order of projection which would result in a coarser filtering operation, the solution coefficients need to be transformed to a modal representation the hierarchical form of which allows for a classification of solution modes based on polynomial degree. The solution can then be coarsely filtered by setting the higher-order modes to zero or by scaling the higher-order coefficients by a factor $\alpha \in [0, 1]$. In this work, we use a cut-off filter order $p^* = 1$ and set the modes of degree greater than one to zero for the test filter. This is equivalent to assuming a test filter to be about twice the width of the grid filter, which is generally followed in finite difference or finite volume methods (Pope 2000). Once the filtered forms of modal solution coefficients are obtained, an inverse transformation is performed to get the filtered nodal solution coefficients thereby obtaining the coarse-filtered solution. In this work, we follow the procedure outlined by Brazell *et al.* (2015) to implement the sharp modal cut-off filter in our solver, and it is discussed in detail in Appendix A.

6.2. Dynamic Smagorinsky model

The dynamic Smagorinsky Model (DSM) is a simple eddy viscosity model that relates the unresolved SGS stresses to the resolved strain-rate \bar{S}_{ij} via a turbulent viscosity ν_{SGS} as

$$\tau_{ij}^{SGS} = 2\bar{\rho}\nu_{SGS}\bar{S}_{ij}, \quad \text{where} \quad \bar{S}_{ij} = \frac{1}{2} \left(\frac{\partial \bar{u}_i}{\partial x_j} + \frac{\partial \bar{u}_j}{\partial x_i} \right). \quad (6.2)$$

The SGS eddy viscosity is related to a characteristic velocity and a length scale on dimensional grounds, and it is given by

$$\nu_{SGS} = (C_S \Delta)^2 |\bar{S}|, \quad (6.3)$$

where C_S is the Smagorinsky coefficient, $|\bar{S}| = \sqrt{2\bar{S}_{ij}\bar{S}_{ij}}$ is the strain-rate magnitude, and Δ is the filter width or a representative grid size. The DSM improves upon the original Smagorinsky model by dynamically adjusting the model coefficient ($C_S \Delta$) based on local flow properties. The idea is to seek a more accurate representation of the turbulence, especially in regions with varying flow conditions. DSM also provides a near-wall correction that can lead to proper near-wall behavior of the SGS viscosity without the use of wall-damping functions. The dynamic calculation of the coefficient is based on an explicitly performed second-level filter operation called the test filter that is applied to the grid-filtered variables.

As mentioned before, we denote the test filter operation by a hat, and we use the sharp modal cut-off filter as the test filter as discussed in 6.1. The model coefficient ($C_s\Delta$) is calculated as

$$(C_s\Delta)^2 = \frac{1}{2} \frac{L_{ij}^d M_{ij}}{M_{kl} M_{kl}}, \quad (6.4)$$

where the Leonard stress tensor L_{ij} and its deviatoric part L_{ij}^d are given by

$$L_{ij} = \widehat{\overline{u_i u_j}} - \widehat{\overline{u_i}} \widehat{\overline{u_j}}, \quad L_{ij}^d = L_{ij} - \frac{1}{3} L_{kk} \delta_{ij}, \quad (6.5)$$

and

$$M_{ij} = |\widehat{\overline{S}}| \widehat{\overline{S}}_{ij} - \Delta_R^2 |\widehat{\overline{S}}| \widehat{\overline{S}}_{ij}. \quad (6.6)$$

The derivative and the test filter operations do not commute for the sharp modal cut-off filter. We follow Brazell *et al.* (2015) to determine the second term of M_{ij} by computing the test-filtered velocity followed by the derivatives of the test-filtered velocity to form the strain-rate tensor. Another possible choice is to use the test filter operation on the grid-filtered strain-rate, but this approach does not have any advantages over the method used here as shown by Brazell *et al.* (2015). The parameter Δ_R is calculated as per the recommendation of Brazell *et al.* (2015) and it is given by

$$\Delta_R = \frac{\widehat{\overline{\Delta_w}}}{\overline{\Delta_w}} = \frac{p+1}{p^*+1}. \quad (6.7)$$

The numerator in Eqn. (6.4) can assume local negative values and this is physically consistent as it corresponds to energy backscatter i.e. energy from the SGS scales is transferred back to the resolved scales. However, negative SGS viscosity values can numerically destabilize the simulation, especially when the sum ($\nu + \nu_{SGS}$) becomes negative. Thus, it is customary to perform some type of averaging of the numerator and denominator, generally in the directions of homogeneity. In this work, we perform two-step averaging. First, the numerator and denominator are averaged over an element to get their representative single values in each element. After this, the numerator and denominator are averaged over the homogeneous directions to get the final averaged numerator and denominator as $\langle L_{ij}^d M_{ij} \rangle$ and $\langle M_{kl} M_{kl} \rangle$, respectively. Finally, the ratio $[0.5(\langle L_{ij}^d M_{ij} \rangle / \langle M_{kl} M_{kl} \rangle)]$ is clipped to get non-negative values.

6.3. Application to statistically stationary channel flows

The new dynamic slip wall model is applied to a series of statistically stationary turbulent channel flows that are homogeneous in directions parallel to the wall. The fully developed turbulent flow between the two parallel walls is separated by a distance 2δ in the z -direction, where δ is the half-channel height. The flow is assumed to be periodic in the stream-wise (x) and span-wise (y) directions. The friction Reynolds number is imposed through a constant forcing in the x -momentum equation using a pressure gradient equal to the wall shear stress $\tau_w = \overline{\rho} u_\tau^2 / \delta$. The simplicity of geometry and boundary conditions makes this canonical flow configuration an appealing test case, and it has been used to validate the performance of previous dynamic slip wall models (Bose & Moin 2014; Bae *et al.* 2019).

The size of the computational domain is $2\pi\delta$ in the x -direction and $\pi\delta$ in the y -direction. The degree of polynomial p used for all the simulations presented here is 2 and the sharp modal cut-off order p^* is 1. For all the cases considered, the flow is initially evolved for

Case	Re_τ	$N_x \times N_y \times N_z$	Δ_x^+	Δ_x/δ	Δ_y^+	Δ_y/δ	Δ_z^+	Δ_z/δ
DSW-2000-G1	1994.756	$8 \times 8 \times 8$	720.68	0.393	360.34	0.196	229.4	0.125
DSW-2000-G2	1994.756	$16 \times 16 \times 16$	360.34	0.196	180.17	0.098	114.7	0.0625
DSW-2000-G3	1994.756	$32 \times 32 \times 32$	180.17	0.098	90.1	0.049	57.35	0.03125
DSW-5200-G1	5185.897	$8 \times 8 \times 8$	1627.35	0.393	813.67	0.196	518	0.125
DSW-5200-G2	5185.897	$16 \times 16 \times 16$	813.67	0.196	406.84	0.098	259	0.0625
DSW-5200-G3	5185.897	$32 \times 32 \times 32$	406.84	0.098	203.42	0.049	129.5	0.03125
DSW-10000-G1	10049	$8 \times 8 \times 8$	3935	0.393	1967.52	0.196	1252.56	0.125
DSW-10000-G2	10049	$16 \times 16 \times 16$	1967.52	0.196	983.76	0.098	626.28	0.0625
DSW-10000-G3	10049	$32 \times 32 \times 32$	983.76	0.098	491.88	0.049	313.14	0.03125

Table 1: Summary of mesh parameters for the different simulated Reynolds numbers.

Here, Δ_x , Δ_y , and Δ_z are the effective grid sizes in the stream-wise (x), span-wise (y), and wall-normal (z) directions, respectively, δ is the half channel height, and Δ_x^+ , Δ_y^+ , and Δ_z^+ are normalized with wall units. N_x , N_y , and N_z represent the number of elements in the stream-wise, span-wise, and wall-normal directions, respectively. The number of degrees of freedom in each direction is given by $(p+1)N_x$, $(p+1)N_y$, and $(p+1)N_z$, where p is the degree of the polynomial basis. Note that the numerical experiments are labeled following the convention [Dynamic slip-wall model (DSW)]-[Re_τ]-[grid resolution].

at least time $20\delta/u_\tau$ units and statistics are sampled for an additional $10\delta/u_\tau$ time units. One-point statistics including the mean velocity and Reynolds shear and normal stresses are compared with the DNS of Lee & Moser (2015) and Hoyas *et al.* (2022).

The performance of the proposed dynamic slip-wall model is validated using the cases listed in Table 1, which shows the simulated Reynolds numbers and the grid resolutions in inner and outer layer units. The meshes are uniform in the stream-wise, span-wise, and wall-normal directions. The first element size in the wall-normal direction for all the considered cases is significantly coarser than a conventional LES mesh and the resolution is insufficient to resolve near-wall turbulent structures. As a result, none of the simulated Reynolds numbers with the grids given in Table 1 are wall-resolved.

A grid sensitivity study for channel flow at $Re_\tau \approx 10000$ is shown in Fig. 1. Starting with a coarse mesh with $8 \times 8 \times 8$ elements, the number of elements in each of the three directions is doubled at each level of refinement. This corresponds to three different coarse near-wall resolutions of $\Delta_z = 0.125\delta$, 0.0625δ , and 0.03125δ i.e. $\Delta_{z_w}^+ \approx 1253$, 626, and 313. The details of the mesh parameters are given in Table 1. For all the cases, the first off-wall grid point lies in the log-layer. The results are plotted starting from the second off-wall element at $(p+1)$ quadrature points in each element. It can be seen that the mean velocity for the coarsest mesh G1 has a slight positive log-layer mismatch which reduces upon grid refinement. The difference between the model predictions at each of the successive grid refinement levels is less than 1%. Grid refinement study for the other two Reynolds number cases shows a similar trend.

A comparison between the dynamic slip-wall model and the equilibrium wall-stress model predictions with the DNS is shown in Fig. 2. The model predictions are obtained on Grid G2 with $16 \times 16 \times 16$ elements. The slope of the mean velocity profiles obtained using the two models is similar, however there is a slight shift between them. Both the mean velocity profile predictions match well with the DNS. The two model predictions for the Reynolds shear stress profiles also match the DNS well. The stream-wise Reynolds stress predicted by the two models is also similar but there is a slight mismatch with the DNS. On the other hand, the span-wise and wall-normal Reynolds stress profiles obtained using the two models closely agree with the DNS.

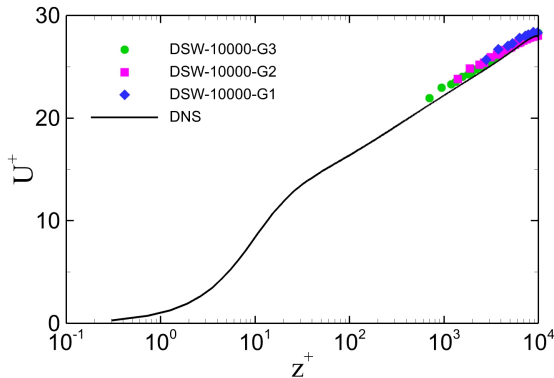
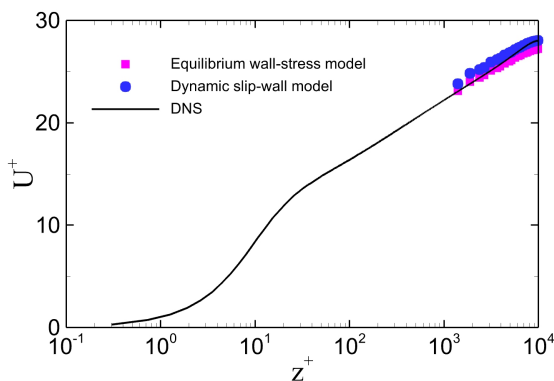
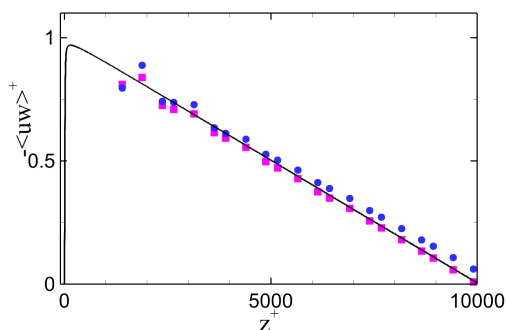


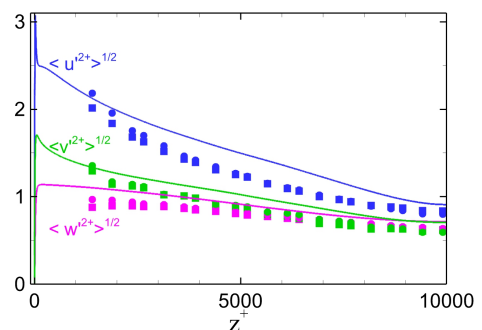
Figure 1: Grid refinement study for the proposed dynamic wall model showing comparisons between model predictions and DNS for the stream-wise mean velocity at $Re_\tau \approx 10000$.



(a)



(b)



(c)

Figure 2: Comparison between the proposed dynamic slip wall model and equilibrium wall-stress model predictions using grid G2 with the DNS for (a) mean velocity, (b) Reynolds shear stress, (c) r.m.s. velocity fluctuations at $Re_\tau \approx 10000$.

A quantitative assessment of the dynamic slip-wall model is performed in terms of the normalized L_2 error in the stream-wise mean velocity U^+ predictions w.r.t the DNS for all the cases presented in Table 1. The calculations exclude the first near-wall element. The normalised L_2 error is determined between the second off-wall element Δ_{2e}^+ and the half

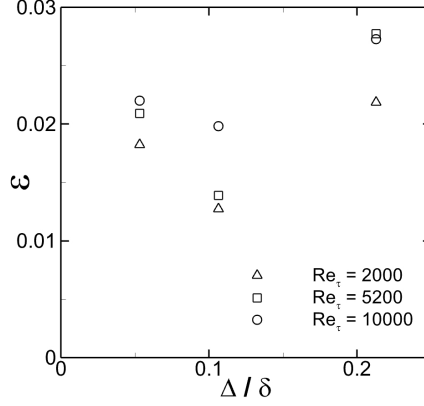


Figure 3: Normalized L_2 error, \mathcal{E} , in stream-wise mean velocity U^+ as a function of grid resolution Δ at $Re_\tau \approx 2000, 5200$, and 10000 .

channel height δ^+ as

$$\mathcal{E} = \left[\frac{\int_{\Delta_{2e}^+}^{\delta^+} (U_{DSW}^+ - U_{DNS}^+)^2 dz^+}{\int_{\Delta_{2e}^+}^{\delta^+} (U_{DNS}^+)^2 dz^+} \right]^{1/2}. \quad (6.8)$$

Here, U_{DSW}^+ and U_{DNS}^+ represent the mean velocity obtained using the proposed dynamic slip-wall model and DNS, respectively. The error is evaluated at $(p + 1)$ quadrature points within each element in the wall-normal direction z^+ , and the integration for each element is performed using quadrature. The error \mathcal{E} is plotted as a function of the representative grid size Δ in Fig. 3. We consider Δ based on element volume, $\Delta = (\Delta_x \Delta_y \Delta_z)^{1/3}$ with Δ_x , Δ_y , and Δ_z taken as the effective grid sizes in the stream-wise, span-wise, and wall-normal directions, respectively. The L_2 error slightly increases with an increase in Reynolds number on an identical grid. However, the maximum error is less than 3% for all the cases considered here demonstrating the performance of the model at practically relevant Reynolds numbers on significantly under-resolved near-wall LES mesh resolutions.

One-point statistics on grid G2 at $Re_\tau \approx 2000, 5200$, and 10000 are presented in Fig. 4 and compared with the available DNS. First and second moments agree well with the DNS at the three Reynolds numbers.

Instantaneous snapshots of the stream-wise slip velocity normalized by the friction velocity u_τ on the bottom wall at $Re_\tau \approx 10000$ employing G2 grid is shown in Fig. 5(a). The mean slip velocity at the wall increases as the Reynolds number increases and the simulation resolves a smaller fraction of the inner layer of the boundary layer. The mean stream-wise slip velocities at the wall are approximately $10.9u_\tau$, $13.9u_\tau$, and $15.35u_\tau$ for $Re_\tau \approx 2000, 5200$, and 10000 , respectively on grid G2; the centerline velocity is approximately $28u_\tau$. This behavior is consistent with the *a priori* filtering tests of Pradhan & Duraisamy (2023) using the optimal finite-element projection framework. The snapshot of vorticity magnitude levels on the bottom wall is also shown. The visualization of the near-wall eddies is shown in Fig. 6 using the Q-criterion.

6.4. Application to separated flows

We next apply the new dynamic slip-wall model to periodic hill flows at different Reynolds numbers. The flow configuration consists of a channel flow with constrictions and forms a generic case of an internal flow separating from a curved surface. Periodic boundary

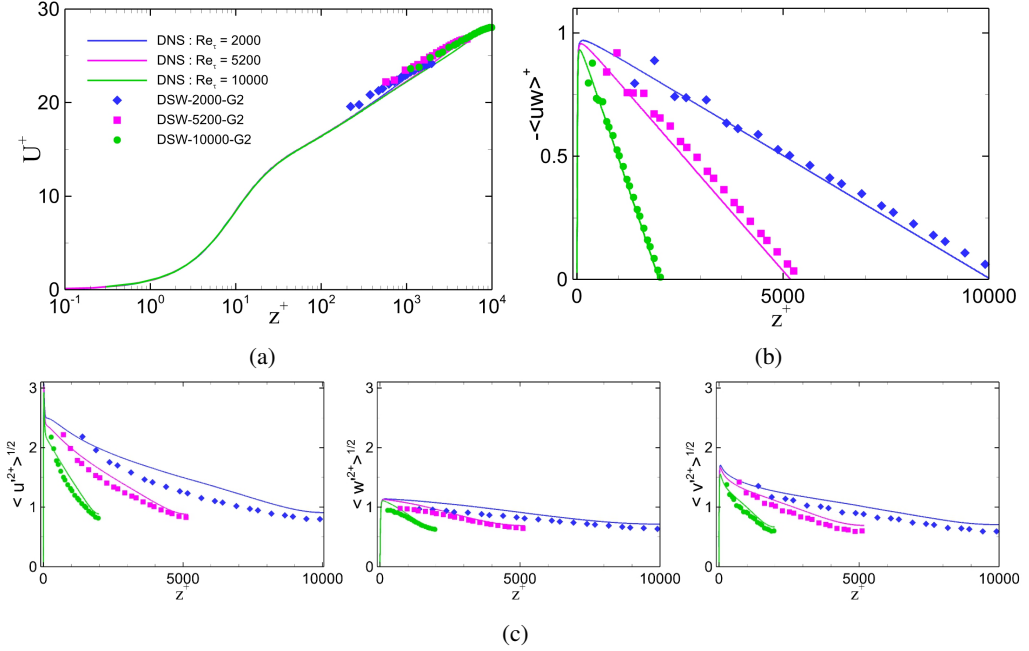


Figure 4: Comparison between DNS and proposed dynamic slip wall model predictions using grid G2 for (a) mean velocity, (b) Reynolds shear stress, (c) r.m.s. velocity fluctuations at $Re_\tau \approx 2000, 5200$, and 10000 .

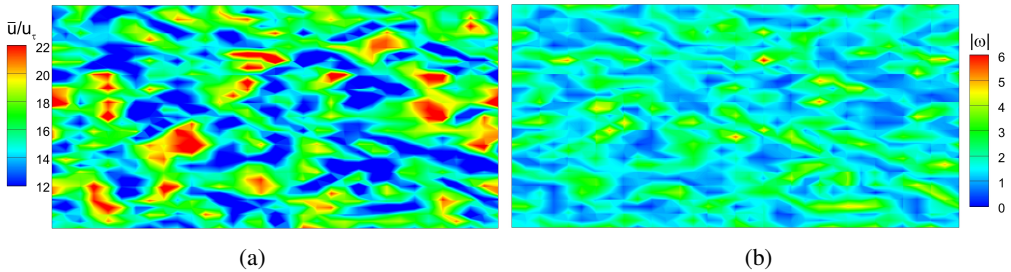


Figure 5: Snapshots of (a) normalized stream-wise slip velocity and (b) vorticity magnitude on the bottom wall obtained using the new dynamic slip-wall model at $Re_\tau \approx 10000$ using grid G2.

conditions applied in the stream-wise (x) and span-wise (y) directions. The flow separates at the hill crest resulting in a large recirculation bubble, and it reattaches further downstream. A Reynolds number based on the bulk velocity at the crest $Re_b = \rho u_b h / \mu$ determines the flow conditions for this case with u_b being the bulk velocity and h the hill height. The constant mass flow rate is ensured by adding a source term in the x -momentum equation. This forcing term is dynamically adjusted to provide the correct mass flow rate at the hill crest, and therefore the correct bulk Reynolds number.

The periodic hill case has been extensively studied over the past 15 years, both experimentally and numerically. Rapp & Manhart (2011) performed experiments in a water channel at Re_b ranging from 5600 to 37000. Several DNS and LES Breuer *et al.* (2009); Diosady & Murman (2014); Krank *et al.* (2018); Gloerfelt & Cinnella (2015); Balakumar *et al.* (2014) studies have also been conducted. Many studies have also been performed to test the

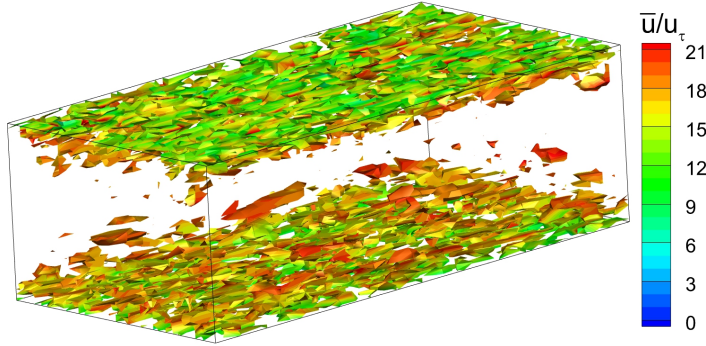


Figure 6: Iso-surfaces of Q-criterion colored with normalized stream-wise velocity \bar{u}/u_τ obtained using the new dynamic slip wall model at $Re_\tau \approx 10000$ case using grid G2.

performance of wall-modelled LES Balakumar *et al.* (2014); Carton de Wiart & Murman (2017). The availability of high-quality data from experiments, DNS, and LES makes this a good benchmark test case to evaluate the performance of the slip-wall model in the presence of separation and reattachment processes.

The size of the computational domain is $L_x = 9h$, $L_y = 4.5h$, and $L_z = 3.035h$ in the streamwise (x), spanwise (y), and wall-normal (z) directions, respectively. Piecewise third-order polynomial functions give the coordinates of the curved hill, and the second hill geometry is described by the same equations with a horizontal translation Rapp & Manhart (2011). We use two grids; a coarse grid with $50 \times 24 \times 9$ elements i.e. $150 \times 72 \times 27$ (≈ 0.2916 million) degrees of freedom and a fine grid with $75 \times 36 \times 15$ elements i.e. $225 \times 108 \times 45$ (≈ 1.1 million) degrees of freedom. In comparison to our grids, a DNS of $Re_b = 10600$ performed by Krank *et al.* (2018) using a 7th order DG solver, used $128 \times 64 \times 64$ elements i.e. $896 \times 448 \times 448$ (≈ 180 million) degrees of freedom whereas to perform an implicit LES, a mesh with $448 \times 224 \times 224$ (≈ 22.5 million) degrees of freedom was used.

The grids are approximately uniform in the stream-wise and span-wise directions and a mild stretching is used in the wall-normal direction. The mesh is perpendicular to the wall in the first cell away from the wall. The effective element sizes at the hill crest, a key region for the periodic hill flow, are $\Delta_x (= \Delta_x^e/p) \approx 0.105h$ and $\Delta_z (= \Delta_z^e/p) \approx 0.093h$ for the coarse grid and $\Delta_x \approx 0.065h$ and $\Delta_z \approx 0.064h$ for the fine grid. Figure 7 shows the two grids used in the computations. We consider two high Reynolds numbers cases of $Re_b = 10600$ and 37000 for which high-quality experimental data is available.

We first study the effect of mesh resolution on the dynamic slip-wall model predictions at $Re_b = 10600$. Wall-normal variation of the mean stream-wise and wall-normal velocity profiles obtained on the coarse and fine grids is shown in Fig. 8 while Reynolds stream-wise, wall-normal, and shear stress profiles are shown in Fig. 9. The model predictions are compared with the experimental data at four stream-wise locations of $x = 1h, 2h, 4h$, and $8h$ which covers the separated as well as post-reattachment regions. The mean stream-wise and wall-normal velocity profile predictions at these locations on the two grids closely match with each other and they compare well with the experimental data. The reverse flow velocities are captured well on these two grids. The Reynolds shear stress profiles on the two grids are also similar to each other and they show a good match with the experiment at the four locations. On the other hand, stream-wise and wall-normal Reynolds stress profile predictions on the coarse grid follow the qualitative trend well and the predictions improve on the fine grid and get closer to the experimental data. It is to note that, despite the very coarse grid resolution,

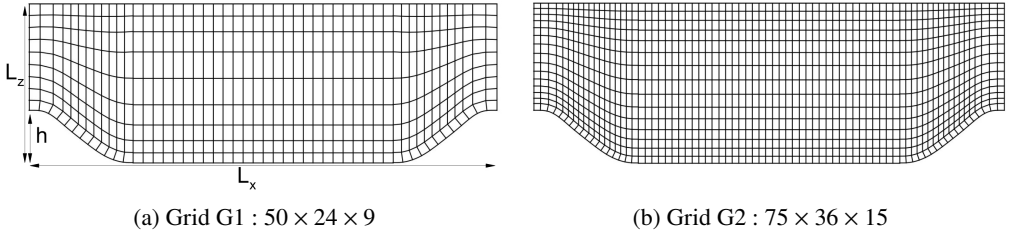


Figure 7: Coarse and fine grids used to compute the periodic hill flows.

the agreement between the resolved part of the Reynolds shear and normal stresses with the measurement is reasonably good.

The periodic hill flow is then computed at a higher Reynolds number of $Re_b = 37000$ using the fine grid and comparisons between the new dynamic slip-wall model and the EQWM predictions for the mean velocities and Reynolds stresses are shown in Figs. 10 and 11, respectively. The EQWM significantly underpredicts the separation and shows a faster recovery and the mean stream-wise and wall-normal velocity profiles in the separated regions show a significant mismatch with the experiments. On the other hand, the dynamic slip-wall model accurately captures the separation and shows an excellent match with the experiments for the mean velocities at the four locations in Fig. 10. The Reynolds shear stress profiles predicted by the dynamic slip-wall model also closely agree with the experiments whereas the EQWM model predictions show a considerable mismatch. This is also the case for the stream-wise Reynolds stress profiles. However, the dynamic slip-wall model predictions for the wall-normal Reynolds stress show some discrepancy with the experiment, but the predictions are considerably better than the EQWM.

7. Conclusion

Several strategies have been proposed to bypass the stringent near-wall grid resolution requirement for performing LES of high Reynolds number flows in the presence of solid walls. In this work, we focus on the slip-wall modeling approach - originally proposed by Bose et al. Bose & Moin (2014) - and replace the conventional no-slip velocity boundary condition with slip velocities at the wall. The major objective is to accurately capture the mean flow characteristics at Reynolds numbers of practical relevance using a significantly coarse near-wall LES mesh, and do so in a robust manner.

We present a new formulation of a dynamic slip-wall model that is consistent with the Discontinuous-Galerkin (DG) framework and is tightly integrated with DG operators. The model coefficients of the modified slip-wall model of Pradhan & Duraisamy (2023) are based on *a priori* estimates obtained using an optimal finite-element projection framework. Here, we propose a dynamic modeling procedure to compute the scaling parameter λ for the slip-wall model coefficient C_w . The dynamic part of the model is based on a modified form of Germano identity and coupled with the dynamic Smagorinsky model. The level of under-resolution is represented by a slip Reynolds number and the proposed model attempts to also incorporate the effects of the numerical discretization and the SGS model.

The canonical case of statistically stationary turbulent channel flow is first used to validate the new dynamic slip-wall model. The model predictions are compared with the available DNS data at three Reynolds numbers of $Re_\tau \approx 2000, 5200, \text{ and } 10000$. Grid independence studies are performed at these Reynolds numbers by considering significantly underresolved LES meshes with stream-wise, span-wise, and wall-normal grid resolutions corresponding to $\Delta_x \approx 0.1 - 0.4\delta$, $\Delta_y \approx 0.05 - 0.2\delta$, and $\Delta_z \approx 0.03 - 0.125\delta$, respectively. These mesh

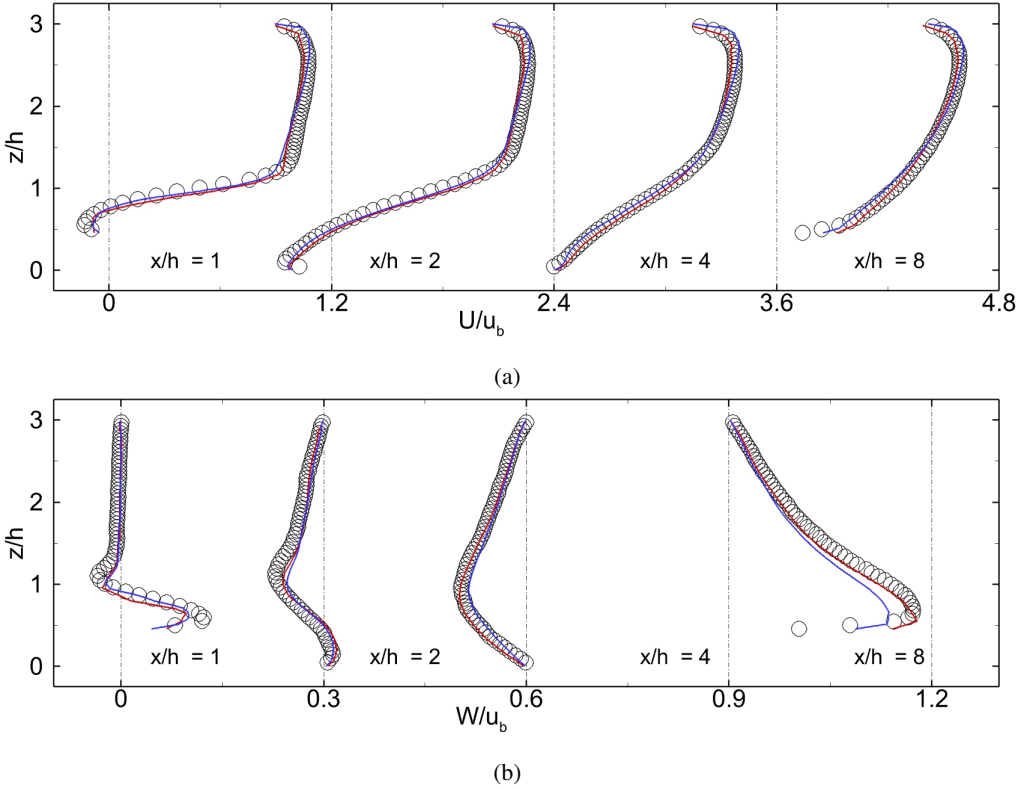


Figure 8: Effect of grid refinement on the mean velocity profiles in the streamwise (U) and vertical (W) directions at different stations for the $Re_b = 10600$ case. Red solid lines, Grid G1; blue solid lines, Grid G2; unfilled circles, Experiment Rapp & Manhart (2011).

resolutions are significantly coarser than the WMLES mesh recommendations of Larsson *et al.* (2016) corresponding to $\Delta_x \approx 0.08\delta$, $\Delta_y \approx 0.05\delta$, and $\Delta_z \approx 0.01 - 0.05\delta$. Mean velocity profiles show an excellent match with the DNS at the considered Reynolds on all the grids with L_2 error less than 3% for all the cases. Reynolds shear and normal stress profiles resolved on the significantly coarse grids also show excellent agreement with the DNS. The model performance is shown to be similar to that of the EQWM, which is known to predict the equilibrium wall-bounded flows without separation accurately. This is a considerable improvement over the dynamic slip-wall model of Bae *et al.* (2019) which shows a significant log-layer mismatch at similar Reynolds numbers but on comparatively finer grid resolutions.

The model performance is evaluated in flow separation and reattachment over periodic hills at Reynolds numbers of $Re_b = 10600$ and 37000 using two different grid resolutions. The meshes used for the computations are significantly coarser than the conventional LES meshes, e.g., the fine mesh used here has about 20 times fewer degrees of freedom than the implicit LES performed by Krank *et al.* (2018). The stream-wise and wall-normal mean velocity profile predictions obtained using the dynamic slip-wall model on the two grids compare well with the experimental data in the separated and post-reattachment flow regions at $Re_b = 10600$. Reynolds shear stress predictions obtained using the two grids also match very well with experiments at different stream-wise locations. However, the Reynolds normal stresses are better predicted on the fine grid. Computations at $Re = 37000$ using the fine grid

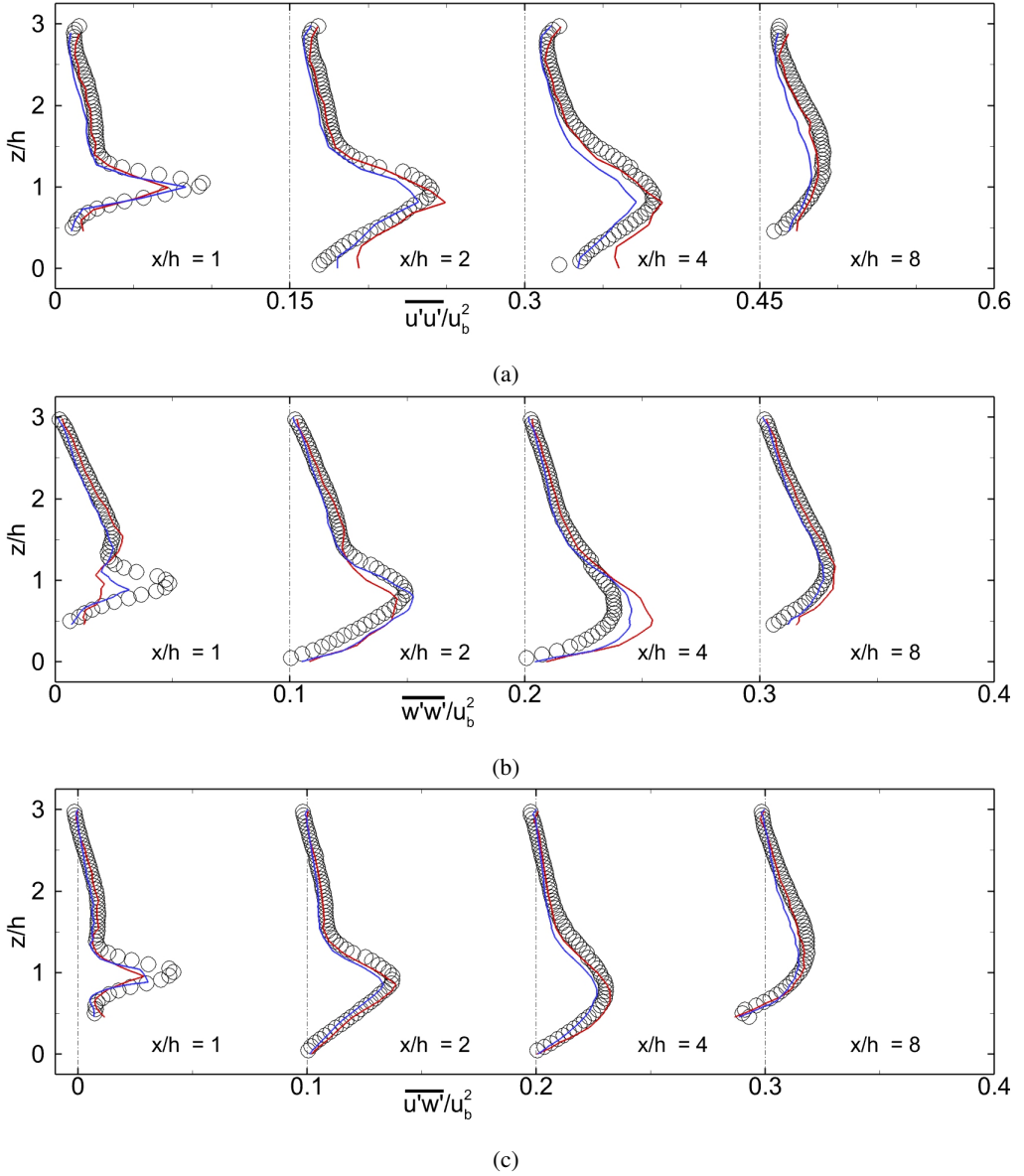


Figure 9: Effect of grid refinement on the Profiles of Reynolds stresses in the streamwise (U) and vertical (W) directions at different stations for the $Re_b = 10600$ case. Red solid lines, equilibrium wall-stress model; Red solid lines, Grid G1; blue solid lines, Grid G2; unfilled circles, Experiment Rapp & Manhart (2011).

show that the dynamic slip-wall model predictions for the mean velocity profiles agree well with the experiments. The Reynolds shear stress profiles are also in excellent agreement with the experiments, with some discrepancies in the Reynolds normal stress predictions. On the other hand, EQWM for this case shows significant discrepancies with the experimental data for the mean velocities as well as Reynolds shear and normal stresses.

The new model can consistently predict mean velocity and Reynolds shear and normal stress profiles for the equilibrium as well as separated flows at high Reynolds numbers using

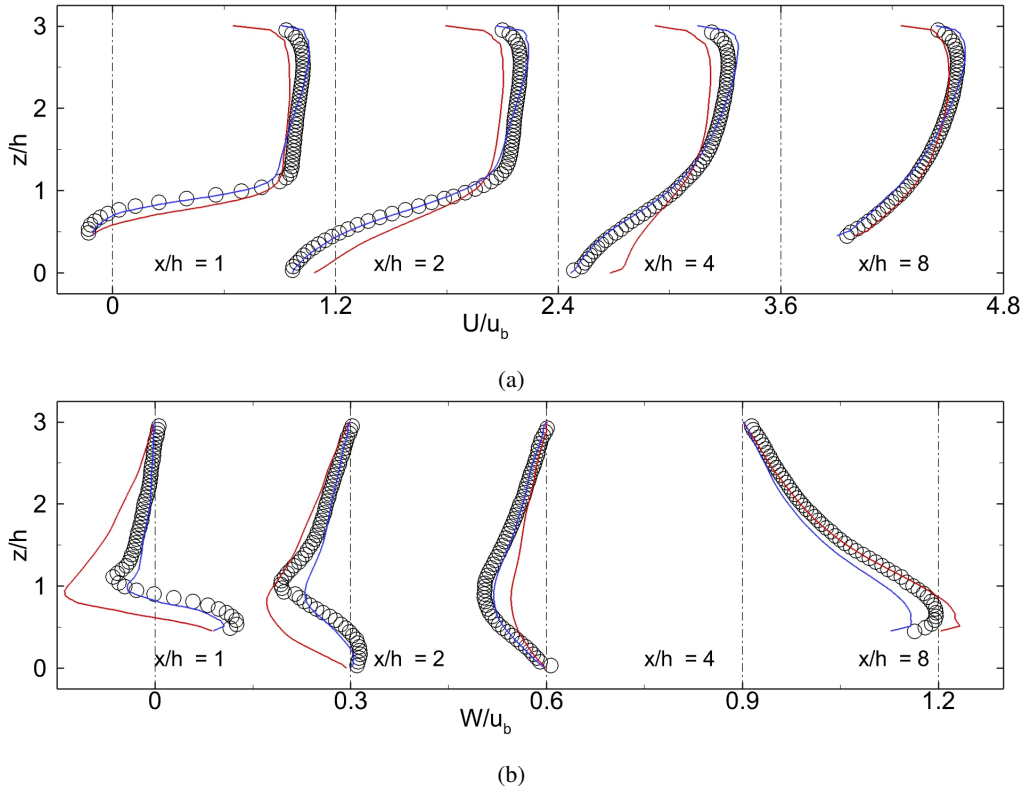


Figure 10: Mean velocity profiles in the streamwise (U) and vertical (W) directions at different stations for the $Re_b = 37000$ case. Red solid lines, equilibrium wall-stress model; blue solid lines, dynamic slip-wall model; unfilled circles, Experiment Rapp & Manhart (2011).

significantly coarse near-wall LES meshes. The model performs at a computational cost similar to the EQWM which is the cheapest state-of-the-art WMLES strategy. In the authors' opinion, the excellent performance of the model may be attributed to the integration of the optimal finite-element projection framework used to obtain the slip-wall parameters with the consistent dynamic procedures for the SGS and slip-wall modeling coupled with the DG framework. This work is a step towards making the slip-wall model a viable computing tool for predicting complex engineering flows.

Acknowledgement

This research was funded by NASA under the project "Scale-resolving turbulence simulations through adaptive high-order discretizations and data-enabled model refinements", grant number 80NSSC18M0149 (Technical monitor: Dr. Gary Coleman). We acknowledge Prof. Krzysztof Fidkowski, Dr. Gary Coleman, and Dr. Aniruddhe Pradhan for their valuable discussions.

Declaration of interests.

The authors report no conflict of interest.

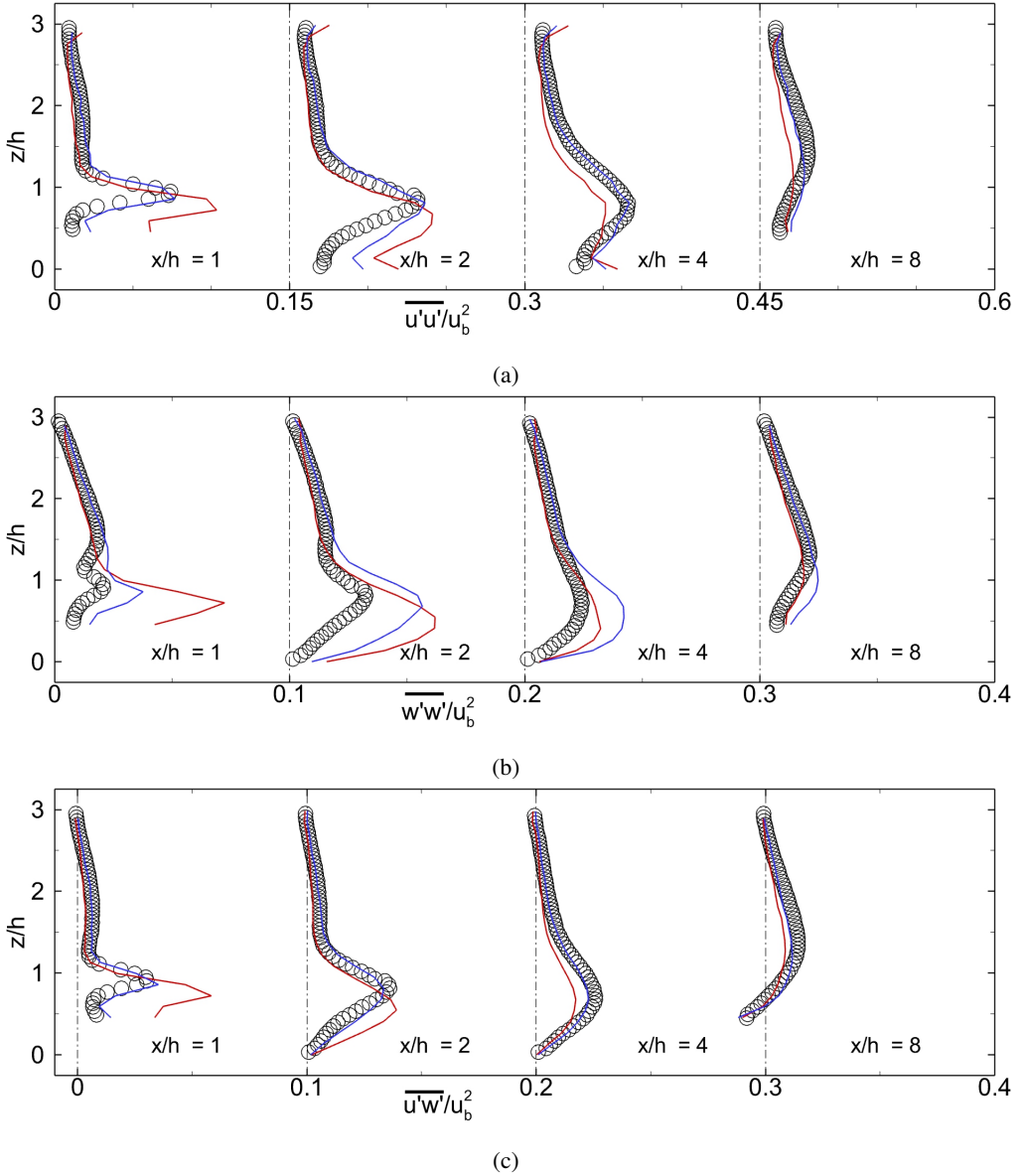


Figure 11: Profiles of Reynolds stresses in the streamwise (U) and vertical (W) directions at different stations for the $Re_b = 37000$ case. Red solid lines, equilibrium wall-stress model; blue solid lines, dynamic slip-wall model; unfilled circles, Experiment Rapp & Manhart (2011).

Appendix A. Sharp modal cut-off filter implementation

The implementation of the sharp modal cut-off filter is a three-step process; transforming the nodal solution coefficients to a hierarchical modal representation, applying a filter on the modal coefficients, and then transforming back into the nodal representation. Let us denote the nodal solution coefficients as u_j , the nodal basis functions as ϕ_j , the modal solution coefficients as b_j , and the modal basis functions as ψ_j . Then, we can write the

approximation u_h to any flow variable u in an element as

$$u \approx u_h = \sum_{j=1}^{p+1} u_j \phi_j = \sum_{j=1}^{p+1} b_j \psi_j. \quad (\text{A } 1)$$

Multiplying the above equation by ψ_i and integrating over the standard element, we get

$$\sum_{j=1}^{p+1} C_{ij} u_j = \sum_{j=1}^{p+1} M_{ij} b_j \quad (\text{A } 2)$$

or in Matrix and vector form, we can write

$$[C] \vec{u} = [M] \vec{b}. \quad (\text{A } 3)$$

Here, the Modal Mass Matrix $[M]$ is given by

$$[M] = M_{ij} = \int_{\Omega_k} \psi_i \psi_j dx. \quad (\text{A } 4)$$

The Mixed Mass Matrix $[C]$ is given by,

$$[C] = C_{ij} = \int_{\Omega_k} \psi_i \phi_j dx. \quad (\text{A } 5)$$

Using Eqn. (A 3), we can obtain the modal solution coefficients, \vec{b} , from the nodal solution coefficients \vec{u} by inverting the Modal Mass Matrix $[M]$ i.e.

$$\vec{b} = [M]^{-1} [C] \vec{u} \quad (\text{A } 6)$$

Now that the hierarchical modal basis coefficients have been obtained, a square filter matrix, $[F]$, can be applied as a matrix-vector product:

$$\widehat{\vec{b}} = [F] \vec{b}, \quad (\text{A } 7)$$

where $\widehat{\vec{b}}$ are the filtered modal solution coefficients. The sharp cut-off Filter matrix $[F]$ is diagonal with its entries being 0 or 1. If all entries are 1 giving the identity matrix, the filtering operation returns the original solution. To obtain a cut-off filter of order $(p^* + 1)$, all diagonal entries of the filter matrix are 1 up to and including the $(p^* + 1)$ diagonal entry with the rest of the entries 0. The last step in the modal decomposition filtering procedure is to transform the filtered modal coefficients back to nodal basis coefficients to give the filtered nodal solution. This reverse transformation can be performed as follows :

$$\widehat{\vec{u}} = [C]^{-1} [M] \widehat{\vec{b}} \quad (\text{A } 8)$$

$$= [C]^{-1} [M] [F] \vec{b} \quad \text{by : Eqn. (A } 7) \quad (\text{A } 9)$$

$$= [C]^{-1} [M] [F] [M]^{-1} [C] \vec{u} \quad \text{by : Eqn. (A } 6) \quad (\text{A } 10)$$

Let

$$[B] = [M]^{-1} [C] \quad \text{and} \quad \widehat{[F]} = [B]^{-1} [F] [B]. \quad (\text{A } 11)$$

We can then write the final filtered nodal solution coefficients as follows :

$$\widehat{\vec{u}} = \widehat{[F]} \vec{u} \quad (\text{A } 12)$$

The final filter matrix $\widehat{[F]}$ can be assembled as a pre-processing step as it does not have a dependence on the solution.

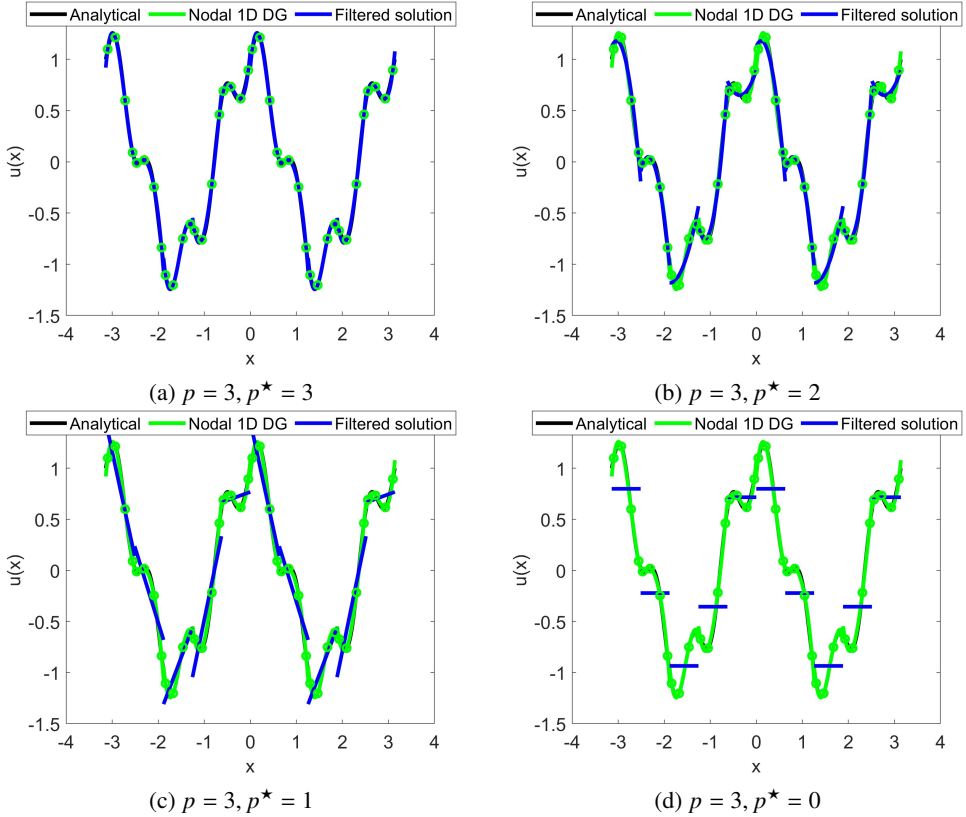


Figure 12: Comparisons of analytical solution for a function $u(x) = \cos(2x) + 0.3\sin(8x)$ in the range $[-\pi, \pi]$ with the best fit obtained using one-dimensional nodal DG employing 10 elements and $p = 3$ along with filtered solutions for $p^* = 0, 1, 2,$ and 3 . Unfilled green circles indicate the quadrature points within each element.

The sharp-modal filter is first tested in a one-dimensional DG set-up. The objective is to find a best-fit for the function $u(x) = \cos(2x) + 0.3\sin(8x)$. The degree of the Lagrange basis function is set to $p = 3$, and the sharp modal cut-off filter is tested for $p^* = 0, 1, 2,$ and 3 . The number of elements used is 10 with 4 quadrature points on each element, and the results are presented in Fig. 12. The analytical solution is plotted for the domain $[-\pi, \pi]$. The nodal DG solution with $p = 3$ matches closely with the analytical solution, and the jumps at the element approximation denote the discontinuous nature of the approximation. The sharp modal cut-off filter with $p^* = 3$ does not affect the solution and the results are identical to the original solution. On the other hand, lower cut-off orders of $p^* = 2, 1,$ and 0 result in a piece-wise quadratic, linear, and constant solution, respectively.

The modal sharp cut-off filter in its 1D form discussed above is extended to 3D in a tensor product fashion and applied before every RK3-TVD step in our in-house DG code. The effect of test filtering operation using the modal sharp cut-off filter on the normalized instantaneous stream-wise velocity \bar{u}/u_δ is shown in Fig. 13. The degree of polynomial used is $p = 3$ and results are shown for $Re_\tau \approx 544$ case with filter orders of $p^* = 3, 2, 1,$ and 0 . The snapshots of \bar{u}/u_τ show the loss of information and decrease in resolution of the flow-field as the filter cut-off order is reduced.

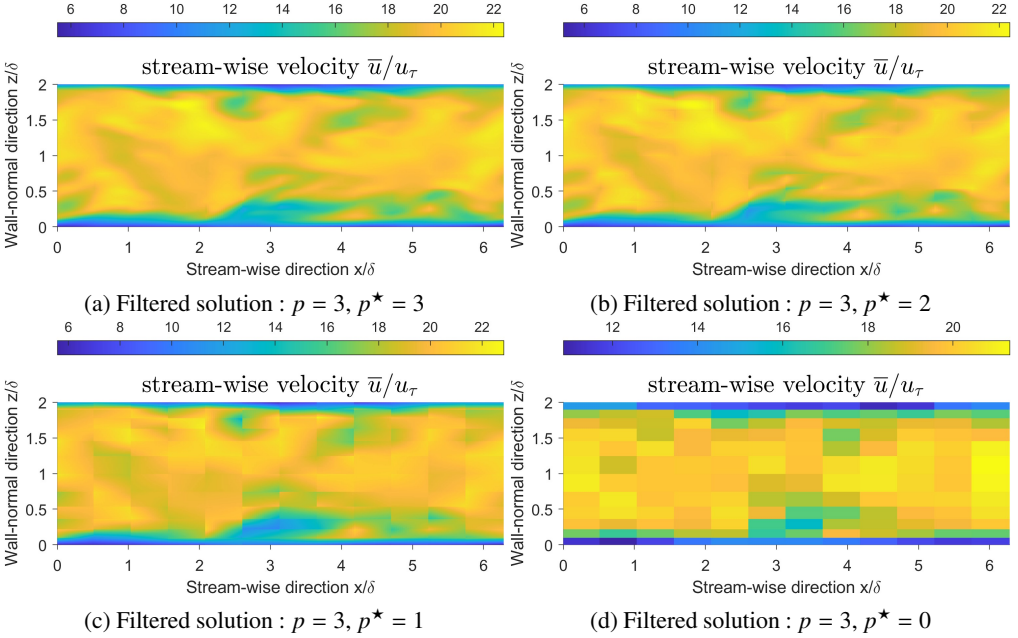


Figure 13: Snapshots of normalized stream-wise velocity in xz plane passing midway through the span-wise domain dimension with $p^* = 3, 2, 1,$ and 0 showing the effects of test filtering operation at $Re_\tau \approx 544$.

Appendix B. Wall-resolved LES at $Re_\tau \approx 544$

We first perform a wall-resolved large eddy simulation (WRLES) for $Re_\tau \approx 544$ channel flow using dynamic Smagorinsky model (DSM) and a constant coefficient Smagorinsky model (CCSM) with $C_s = 0.12$. The mesh size is $36 \times 30 \times 24$ elements in the stream-wise, span-wise, and wall-normal directions, respectively. The grid is uniform in the stream-wise and span-wise directions and it is geometrically stretched in the wall-normal direction with a stretching ratio of 1.2. The effective grid sizes in each direction in wall units are $\Delta_x^+ \approx 38$, $\Delta_y^+ \approx 19$, and Δ_z^+ at the wall is $\Delta_{z_w}^+ \approx 4.5$ and at the channel center is $\Delta_{z_c}^+ \approx 32.2$. The grid resolution is based on the recommendation of Bose & Moin (2014) for a wall-resolved LES, i.e. $\Delta_x^+ \lesssim 50$, $\Delta_y^+ \lesssim 30$, and $\Delta_{z_w}^+ \sim O(1)$. In comparison, the grid resolution of the available DNS (Lee & Moser 2015) is $\Delta_x^+ \approx 8.9$, $\Delta_y^+ \approx 5$, $\Delta_{z_w}^+ \approx 0.019$, and $\Delta_{z_c}^+ \approx 4.5$. Please note that, the effective grid sizes Δ_x , Δ_y and Δ_z for the finite element grid are defined as $\Delta_x = \Delta_x^e/p$, $\Delta_y = \Delta_y^e/p$, and $\Delta_z = \Delta_z^e/p$, respectively. The quantities Δ_x^e , Δ_y^e , and Δ_z^e represent the actual element sizes in the finite element mesh.

The instantaneous stream-wise velocity \bar{u} normalized with u_τ for the CCSM and DSM SGS models in a xz -plane are shown in Fig. 14. The solution for both cases is reasonably resolved. Snapshots of the vorticity magnitude on the bottom wall are shown in Fig. 15. DSM predicts higher levels of the vorticity magnitude compared to the CCSM. On the other hand, Fig. 16 shows the isometric view of the iso-surfaces of the Q-criterion for the two SGS models to visualize the near-wall eddies.

The wall-normal variation of the mean Smagorinsky coefficient $\langle C_s \rangle$ along with mean velocity and Reynolds shear and normal stresses for the DSM and CCSM SGS models compared with the DNS is shown in Fig. 17. The Smagorinsky coefficient C_s for the DSM assumes a value of zero at the wall as L_{ij}^d in Eqn. (6.4) is equivalently zero at the wall owing to the no-slip velocity boundary condition. It gradually increases in the viscous-sublayer before

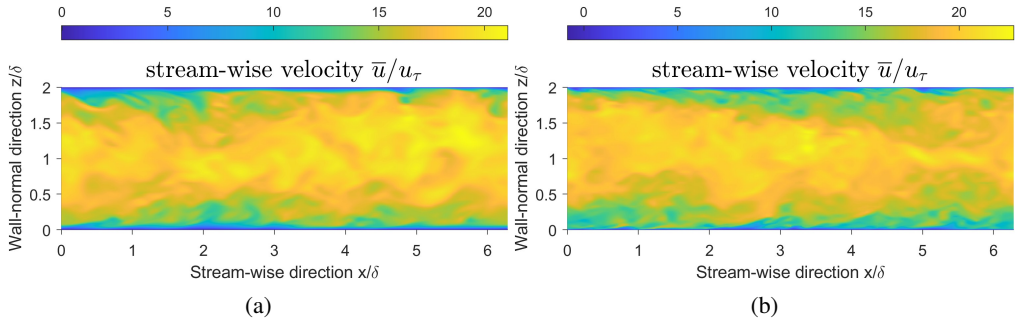


Figure 14: Snapshots of normalized stream-wise velocity in a xz plane passing midway through the span-wise dimension for a WRLES at $Re_\tau \approx 544$ obtained using (a) CCSM and (b) DSM SGS models.

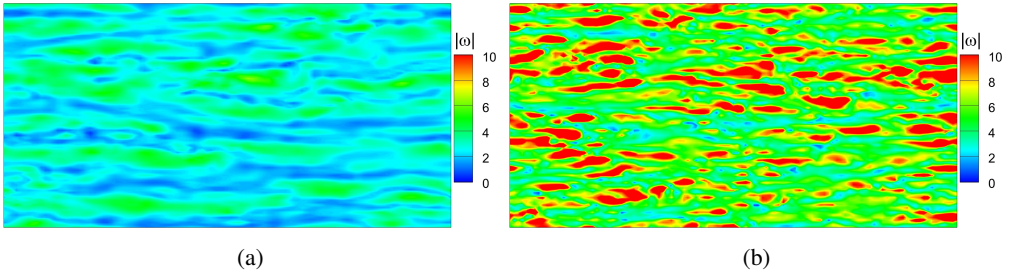


Figure 15: Snapshots of vorticity magnitude on the bottom wall for a WRLES at $Re_\tau \approx 544$ obtained using (a) CCSM and (b) DSM SGS models.

reaching a value of about 0.12 in the log-layer at about $z^+ \approx 60$ after which it remains close to 0.1 – 0.12 till the half channel height δ^+ . The dynamic adjustment of C_s including the proper near-wall behavior results in the mean velocity and Reynolds shear and normal stress profiles that are almost identical to the DNS data. On the other hand, CCSM uses a constant value of 0.12 for the Smagorinsky coefficient everywhere in the flow-field, and unlike the DSM, near-wall damping of C_s and hence ν_{SGS} is not present. This results in incorrect Reynolds shear and normal stress profiles and the mean velocity profile shows a significant negative off-set compared to the DNS as seen in Fig. 17. The results clearly suggest that DSM gives a better performance compared to CCSM on the same grid and thus is a better choice as the SGS model. Going forward, we will use DSM as the SGS model for all the computations.

Appendix C. Sensitivity analysis

The proposed dynamic slip wall model involves two model parameters, namely C_{wR} and Δ_R . The definition of the filter operation fixes the value of Δ_R , which is the ratio of the test filter width to the grid filter width. We have used a value for Δ_R as recommended by Brazell *et al.* (2015). Numerical experiments using different values for Δ_R in the plausible range of $\Delta_R = [1, 2]$ for $p = 2$ and $p^* = 1$ resulted in negligible differences in the results and these observations are similar to those made by Bae *et al.* (2019) for their dynamic slip wall model. On the other hand, the parameter C_{wR} comes into the picture because of the use of different values of the model coefficient C_w at the test filter and grid filter levels. The sensitivity to C_{wR} is tested for values in the plausible range $C_{wR} = [1, 2]$. Results for the two extreme values in this range i.e. $C_{wR} = 1$ and 2 are shown in Fig. 18 for $Re_\tau \approx 10000$ case obtained using grid G2. The effect of C_{wR} on the mean velocity and Reynolds stress predictions is

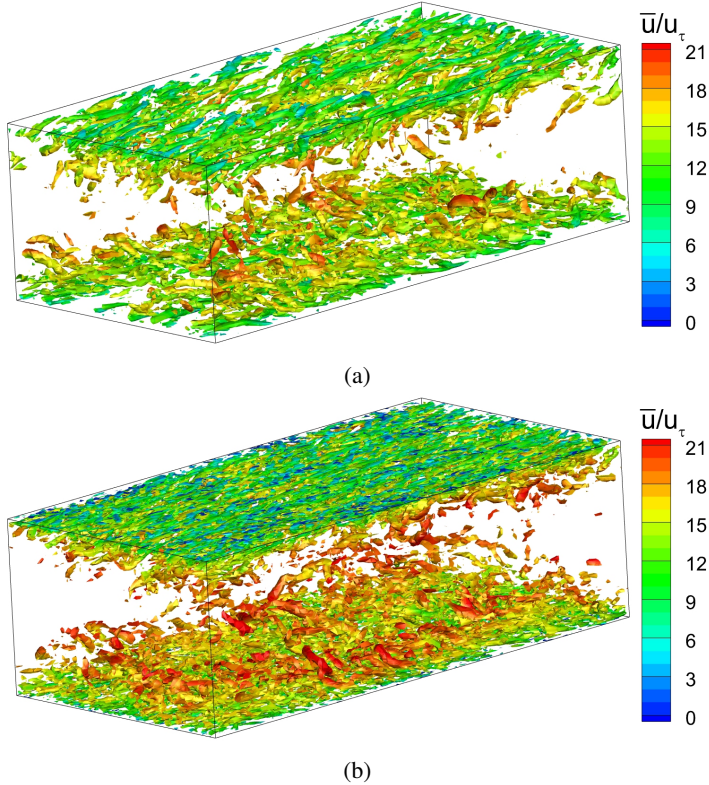


Figure 16: Iso-surfaces of Q-criterion colored with normalized stream-wise velocity \bar{u}/u_τ for a WRLES at $Re_\tau \approx 544$ obtained using (a) CCSM and (b) DSM SGS models.

also found to be negligible and the results are almost identical. This suggests that the model coefficient C_w can be taken to be the same at the test and grid filtered levels, which is the general practice (Bose & Moin 2014; Bae *et al.* 2019)

Appendix D. Computational cost

The simulations were performed on NASA's Pleiades Supercomputer on the Broadwell compute nodes consisting of E5-2680v4 Intel Xeon processors at 2.4 GHz. For the channel flow computations on the finest mesh G3 consisting of $32 \times 32 \times 32$ elements with about 0.885 million degrees of freedom, the dynamic slip-wall model takes about 0.135s of wall time per time-step on 512 processors. For the $Re_\tau \approx 10000$ case, the dynamic slip-wall model requires about wall time of 11.8 mins for a single flow-through ($= L_x/U_b$) on the grid G3. On the other hand, for the periodic hill cases using the fine grid consisting of $75 \times 36 \times 15$ elements with about 1.1 million degrees of freedom, the wall time required by the dynamic slip-wall model per time-step is approximately 0.088s on 3330 processors. For the $Re_b = 37000$ case, the wall time required for a single flow-through is about 22 mins. The equilibrium wall-stress model requires a similar time per time-step as that of the dynamic slip-wall model for the channel flow and periodic hill cases on identical grids.

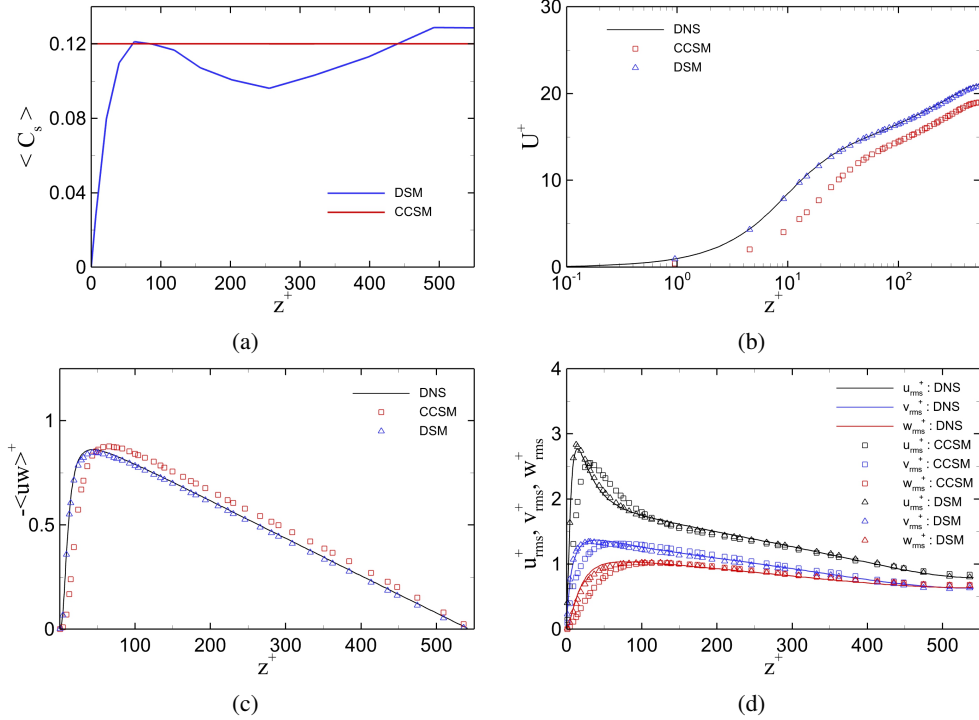


Figure 17: Wall-normal variation of (a) mean Smagorinsky coefficient $\langle C_s \rangle$, (b) mean velocity, (c) Reynolds shear stress, and (d) r.m.s. velocity fluctuations for a wall-resolved LES employing DSM and CCSM as the SGS models compared with the DNS at $Re_\tau \approx 544$.

REFERENCES

- BAE, HYUNJI JANE, LOZANO-DURÁN, ADRIÁN, BOSE, SANJEEB T & MOIN, PARVIZ 2019 Dynamic slip wall model for large-eddy simulation. *Journal of fluid mechanics* **859**, 400–432.
- BALAKUMAR, P, PARK, GI & PIERCE, B 2014 Dns, les, and wall-modeled les of separating flow over periodic hills. In *Proceedings of the Summer Program*, pp. 407–415.
- BASSI, F & REBAY, S 2000 Gmres discontinuous galerkin solution of the compressible navier-stokes equations. In *Discontinuous Galerkin Methods: Theory, Computation and Applications*, pp. 197–208. Springer.
- BOSE, SANJEEB T & MOIN, PARVIZ 2014 A dynamic slip boundary condition for wall-modeled large-eddy simulation. *Physics of Fluids* **26** (1), 015104.
- BRAZELL, MATTHEW J, BRAZELL, MICHAEL J, STOELLINGER, MICHAEL K & MAVRIPLIS, DIMITRI J 2015 Using les in a discontinuous galerkin method with constant and dynamic sgs models. In *53rd AIAA Aerospace Sciences Meeting*, p. 0060.
- BREUER, MICHAEL, PELLER, NIKOLAUS, RAPP, CH & MANHART, MICHAEL 2009 Flow over periodic hills—numerical and experimental study in a wide range of reynolds numbers. *Computers & Fluids* **38** (2), 433–457.
- CABOT, W & MOIN, PARVIZ 2000 Approximate wall boundary conditions in the large-eddy simulation of high reynolds number flow. *Flow, Turbulence and Combustion* **63**, 269–291.
- CHOI, JUNG-IL, EDWARDS, JACK R & BAURLE, ROBERT A 2009 Compressible boundary-layer predictions at high reynolds number using hybrid les/rans methods. *AIAA journal* **47** (9), 2179–2193.
- DAVIDSON, LARS & BILLSON, MATTIAS 2006 Hybrid les-rans using synthesized turbulent fluctuations for forcing in the interface region. *International journal of heat and fluid flow* **27** (6), 1028–1042.
- DAVIDSON, LARS & DAHLSTRÖM, SIMON 2005 Hybrid les-rans: An approach to make les applicable at high reynolds number. *International journal of computational fluid dynamics* **19** (6), 415–427.

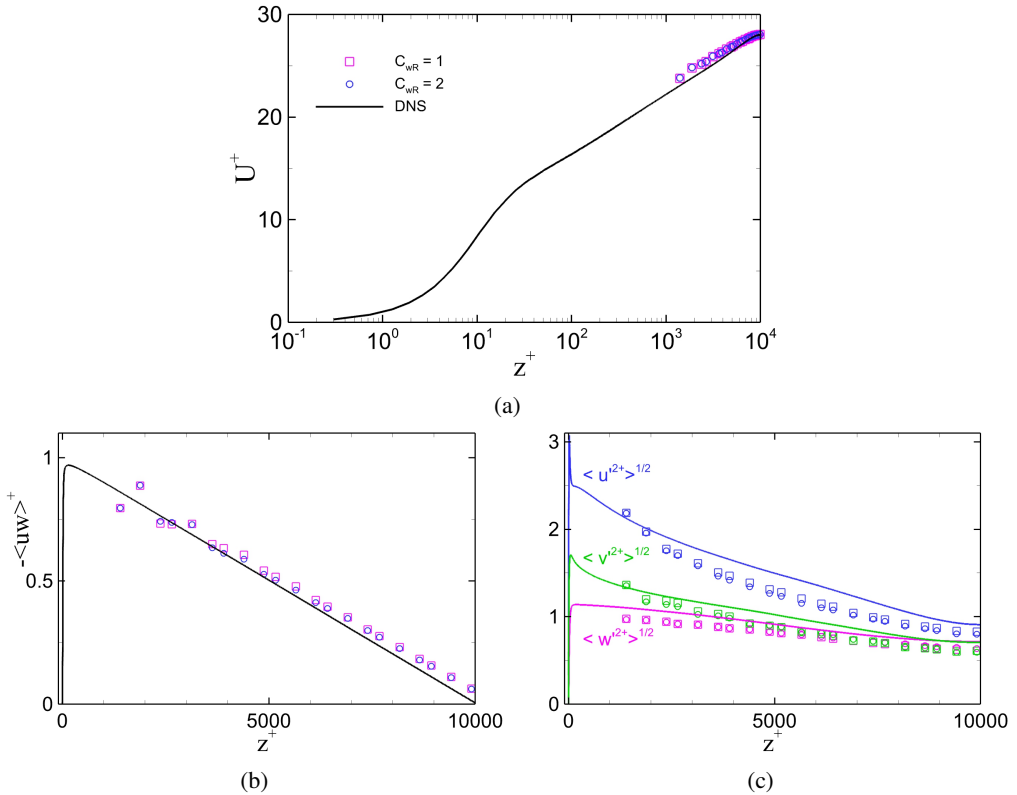


Figure 18: Effect of the parameter C_{wR} values on the proposed dynamic wall model predictions for the case DSW-10000-G2 along with DNS comparisons for (a) mean velocity, (b) Reynolds shear stress, and (c) r.m.s. velocity fluctuations.

- DIOSADY, LASLO T & MURMAN, SCOTT M 2013 Design of a variational multiscale method for high reynolds number compressible flows. In *21st AIAA Computational Fluid Dynamics Conference*, p. 2870.
- DIOSADY, LASLO T & MURMAN, SCOTT M 2014 Dns of flows over periodic hills using a discontinuous galerkin spectral-element method. In *44th AIAA Fluid Dynamics Conference*, p. 2784.
- GASSNER, GREGOR J & BECK, ANDREA D 2013 On the accuracy of high-order discretizations for underresolved turbulence simulations. *Theoretical and Computational Fluid Dynamics* **27** (3-4), 221–237.
- GERMANO, MASSIMO 1986 Differential filters of elliptic type. *The Physics of fluids* **29** (6), 1757–1758.
- GERMANO, M 1990 Averaging invariance of the turbulent equations and similar subgrid scale modeling. *CTR Manuscript* **116**.
- GERMANO, MASSIMO, PIOMELLI, UGO, MOIN, PARVIZ & CABOT, WILLIAM H 1991 A dynamic subgrid-scale eddy viscosity model. *Physics of Fluids A: Fluid Dynamics* **3** (7), 1760–1765.
- GLOERFELT, XAVIER & CINNELLA, PAOLA 2015 Investigation of the flow dynamics in a channel constricted by periodic hills. In *45th AIAA Fluid Dynamics Conference*, p. 2480.
- GOC, KONRAD, BOSE, SANJEEB & MOIN, PARVIZ 2020 Wall-modeled large eddy simulation of an aircraft in landing configuration. In *AIAA Aviation 2020 Forum*, p. 3002.
- GOC, KONRAD A, LEHMKUHL, ORIOL, PARK, GEORGE ILHWAN, BOSE, SANJEEB T & MOIN, PARVIZ 2021 Large eddy simulation of aircraft at affordable cost: a milestone in computational fluid dynamics. *Flow* **1**, E14.
- HEINZ, STEFAN 2020 A review of hybrid rans-les methods for turbulent flows: Concepts and applications. *Progress in Aerospace Sciences* **114**, 100597.
- HOYAS, SERGIO, OBERLACK, MARTIN, ALCÁNTARA-ÁVILA, FRANCISCO, KRAHEBERGER, STEFANIE V & LAUX,

- JONATHAN 2022 Wall turbulence at high friction reynolds numbers. *Physical Review Fluids* **7** (1), 014602.
- KAWAI, SOSHI & LARSSON, JOHAN 2012 Wall-modeling in large eddy simulation: Length scales, grid resolution, and accuracy. *Physics of Fluids* **24** (1), 015105.
- KEATING, ANTHONY & PIOMELLI, UGO 2006 A dynamic stochastic forcing method as a wall-layer model for large-eddy simulation. *Journal of Turbulence* (7), N12.
- KRANK, BENJAMIN, KRONBICHLER, MARTIN & WALL, WOLFGANG A 2018 Direct numerical simulation of flow over periodic hills up to $re_h = 10,595$. *Flow, turbulence and combustion* **101**, 521–551.
- LARSSON, JOHAN, KAWAI, SOSHI, BODART, JULIEN & BERMEJO-MORENO, IVAN 2016 Large eddy simulation with modeled wall-stress: recent progress and future directions. *Mechanical Engineering Reviews* **3** (1), 15–00418.
- LEE, MYOUNGKYU & MOSER, ROBERT D 2015 Direct numerical simulation of turbulent channel flow up to. *Journal of fluid mechanics* **774**, 395–415.
- LEHMKUHL, O, PARK, GI, BOSE, ST & MOIN, P 2018 Large-eddy simulation of practical aeronautical flows at stall conditions. *Proceedings of the 2018 Summer Program, Center for Turbulence Research, Stanford University* **87**.
- MOIN, PARVIZ & MAHESH, KRISHNAN 1998 Direct numerical simulation: a tool in turbulence research. *Annual review of fluid mechanics* **30** (1), 539–578.
- NICOUD, FRANCK, BAGGETT, JS, MOIN, PARVIZ & CABOT, WILLIAM 2001 Large eddy simulation wall-modeling based on suboptimal control theory and linear stochastic estimation. *Physics of fluids* **13** (10), 2968–2984.
- PARK, GI & MOIN, P 2016 Wall-modeled les: Recent applications to complex flows. *Annual Research Briefs* pp. 39–50.
- PIOMELLI, UGO & BALARAS, ELIAS 2002 Wall-layer models for large-eddy simulations. *Annual review of fluid mechanics* **34** (1), 349–374.
- PIOMELLI, UGO, BALARAS, ELIAS, PASINATO, HUGO, SQUIRES, KYLE D & SPALART, PHILIPPE R 2003 The inner–outer layer interface in large-eddy simulations with wall-layer models. *International Journal of heat and fluid flow* **24** (4), 538–550.
- POPE, STEPHEN B 2000 *Turbulent flows*. Cambridge university press.
- PRADHAN, ANIRUDDHE & DURAISAMY, KARTHIK 2023 A unified understanding of scale-resolving simulations and near-wall modelling of turbulent flows using optimal finite-element projections. *Journal of Fluid Mechanics* **955**, A6.
- RAPP, CH & MANHART, M 2011 Flow over periodic hills: an experimental study. *Experiments in fluids* **51** (1), 247–269.
- REICHARDT, HANS 1951 Vollständige darstellung der turbulenten geschwindigkeitsverteilung in glatten leitungen. *ZAMM-Journal of Applied Mathematics and Mechanics/Zeitschrift für Angewandte Mathematik und Mechanik* **31** (7), 208–219.
- ROE, PHILIP L 1981 Approximate riemann solvers, parameter vectors, and difference schemes. *Journal of computational physics* **43** (2), 357–372.
- SAGAUT, PIERRE 2005 *Large eddy simulation for incompressible flows: an introduction*. Springer Science & Business Media.
- SHUR, MIKHAIL L, SPALART, PHILIPPE R, STRELETS, MIKHAIL KH & TRAVIN, ANDREY K 2008 A hybrid rans-les approach with delayed-des and wall-modelled les capabilities. *International journal of heat and fluid flow* **29** (6), 1638–1649.
- SLOTNICK, JEFFREY P, KHODADOUST, ABDOLLAH, ALONSO, JUAN, DARMOFAL, DAVID, GROPP, WILLIAM, LURIE, ELIZABETH & MAVRIPLIS, DIMITRI J 2014 Cfd vision 2030 study: a path to revolutionary computational aerospace. *Tech. Rep. NASA/CR-2014-218178*.
- SMITS, ALEXANDER J & MARUSIC, IVAN 2013 Wall-bounded turbulence. *Physics Today* **66** (9), 25–30.
- TEMPLETON, JEREMY A, WANG, MENG & MOIN, PARVIZ 2006 An efficient wall model for large-eddy simulation based on optimal control theory. *Physics of Fluids* **18** (2).
- TEMPLETON, JEREMY A, WANG, MENG & MOIN, PARVIZ 2008 A predictive wall model for large-eddy simulation based on optimal control techniques. *Physics of Fluids* **20** (6).
- CARTON DE WIART, CORENTIN & MURMAN, SCOTT M 2017 Assessment of wall-modeled les strategies within a discontinuous-galerkin spectral-element framework. In *55th AIAA Aerospace Sciences Meeting*, p. 1223.
- WILCOX, DAVID C & OTHERS 1998 *Turbulence modeling for CFD*, , vol. 2. DCW industries La Canada, CA.